University of Alberta

Strong Coupling and Coherent Phenomena in Semiconductor Metamaterials

by

Prashant Shekhar

A thesis submitted to the Faculty of Graduate Studies and Research in partial fulfillment of the requirements for the degree of

Master of Science
in
Photonics and Plasmas

Electrical and Computer Engineering

Spring 2014
Edmonton,Alberta

I would like dedicate this work to my mother, Alka Shekhar, and my father, Tushar Shekhar, for teaching me all that is truly important

Abstract

Metamaterials are nanoengineered materials with electromagnetic properties beyond those found in nature. Recently, interest has focused towards controlling light matter interaction using metamaterials for applications in nanoscale emitters from lasers to single photon sources. We propose an active metamaterial with embedded quantum wells that strongly interact with unique electromagnetic modes of the nanostructured medium. This strong interaction is characterized by the phenomenon of strong coupling wherein the modes of a metamaterial show energy splitting at the intersubband transition wavelength of the embedded quantum wells. Additionally, we show that semiconductor metamaterials can mediate superradiant behaviour between a pair of emitters across distances greater than their radiation wavelength. This work paves the way for realizing quantum strong coupling and coherent effects in semiconductor metamaterial structures.

Acknowledgements

I would like to thank and acknowledge the members of my research group: Jon Atkinson, Cris Cortes, Yu Guo, Huan Hu, Saman Jahani, Sean Molesky and Ward Newman. Their knowledge, suggestions, criticisms and, most importantly, their friendship made completing this thesis possible. Each of their contributions is greatly appreciated.

I would also like to give a special thank-you to my supervisor Professor Zubin Jacob, not only for his vast knowledge and contribution to this work but also his thoughtful insight, detailed guidance, and consistent encouragement throughout the entire project.

Last but not least, I would like to thank my family: my parents Alka Shekhar and Tushar Shekhar and my sister Natasha Shekhar for their unwavering encouragement and support in all of my endeavours.

Contents

List of Figures

List of Tables

List of Abbreviations and Symbols

Abbreviation	Extended Form
EMT	Effective Medium Theory
ENZ	Epsilon-Near-Zero
HMM	Hyperbolic Metamaterial
ISBT	Intersubband Transition
LDOS	Local Density of States
MQW	Multiple Quantum Well
OTT	Optical Topological Transition
PDOS	Photonic Density of States
SPP	Surface Plasmon Polariton
λ	Wavelength
$\Re$	Real Component of Expression
$\Im$	Imaginary Component of Expression

Chapter 1

Introduction

Developments in the field of nanotechnology have allowed the continued improvement of the design and fabrication of artificial structures. Recently, synthesized structures with subwavelength building blocks, known as metamaterials, have shown promise for engineering nanoscale light-matter interactions [1, 2]. The subwavelength components of the metamaterial structure allow for unique electromagnetic responses as a result of the near-field coupling between them. Metamaterials have been shown to have novel applications such as negative refraction [3] and subwavelength imaging [4, 5].

Chapter 2 looks at a special class of metamaterial known as hyperbolic metamaterials or HMMs [6]. HMM structures are fabricated with subwavelength metal and dielectric components that allow them to achieve an extremely anisotropic dielectric tensor. This extreme anisotropy results in a unique hyperbolic dispersion for such materials from where they derive their name. Such a unique dispersion does not occur in nature at optical and mid-IR frequencies. The hyperbolic dispersion of the structure leads to novel phenomena such as the ability to support subwavelength modes as well as a large photonic density of states [7, 8]. Chapter 2 lays the groundwork and establishes the origin of the characteristic hyperbolic dispersion of these metal-dielectric structures.

HMMs have shown a lot of promise in the optical regime garnering a large amount of interest amongst researchers [1, 4, 5, 8, 9]. Chapter 3 looks at the application of hyperbolic metamaterials in the mid-IR. We look specifically at designing HMMs composed of semiconductors rather than the more commonly used plasmonic metals such as silver and gold. Furthermore, chapter 3 discusses using semiconductors for embedding quantum wells within the HMM. This can lead to strong coupling interactions between the HMM and the quantum wells. Although strong coupling has been observed in a multitude of systems such as photonic crystals and microcavities,

it has not been fully understood for lossy metamaterial systems. We will see that strong coupling is a stepping stone to realizing novel quantum phenomena in such hyperbolic structures.

Chapter 4 looks into mediating superradiant behaviour between a pair of emitters over large distances using a hyperbolic metamaterial. Superradiant phenomena involves a collection of emitters radiating as a single ensemble, such that their collective spontaneous decay rate is coherently increased [10]. The original work was completed by Dicke in 1954 and recently, superradiance has garnered interest for determining specific atomic states and controlling and measuring entanglement between multiple emitters [11]. In vacuum, superradiance is induced through the near-field interactions of very closely spaced emitters, much closer than their wavelength of radiation. We will see, in the preliminary work, that superradiance over much larger distances can be achieved by using the HMM to induce such coherent effects.

This thesis predicts two new phenomena pertinent to the field hyperbolic metamaterials: strong coupling and superradiance. Our analysis follows a semiclassical approach and lays the foundation for future quantum optical treatment of both phenomena.

Chapter 2

Hyperbolic Metamaterials

Recent achievements in nanotechnology have helped usher in a new class of artificial media with subwavelength building blocks known as metamaterials. These novel metamaterials rely not only on the resonant nature of the structures but also the subwavelength coupling between their constituent components[1, 2]. This allows one to engineer unique electromagnetic responses for controlling light-matter interaction at the nanoscale. Here, we define and characterize a special class of such artificial media known as hyperbolic metamaterials.

The term hyperbolic is derived from the hyperbolic isofrequency dispersion inherent in the structures as opposed to the spherical or ellipsoidal isofrequency surface property seen in conventional materials. In this chapter, we will see how the hyperbolic dispersion is achieved as well as practical approaches to fabricate such structures. Finally, the unique properties of the hyperbolic metamaterials, such as their ability to support subwavelength modes as well as their large photonic density of states will be discussed.

2.1 Dispersion of Plane Waves in a Uniaxial Medium

The nature of hyperbolic dispersion, as detailed in section 2.2, can be understood by first looking at the dispersion relation of plane waves in a conventional uniaxial medium. Maxwell's equations for time dependent electric and magnetic fields (equation 2.1), once decoupled, provide the wave equations for electromagnetic waves.

$$\nabla^2 + \frac{\bar{\mu}\bar{\epsilon}}{c^2}\frac{\partial^2}{\partial t^2}\begin{pmatrix}\vec{E}\\ \vec{B}\end{pmatrix} = 0 \tag{2.1}$$

$\bar{\mu}$ and $\bar{\epsilon}$ are tensors that represent the magnetic permeability and the electric permittivity respectively and c is the speed of light in vacuum. If the material has no magnetic response, we can represent the magnetic permeability tensor with the

identity tensor, $\bar{\mu} = \bar{I}$, which is true for all naturally occurring media at optical frequencies [12]. For an anisotropic material with a uniaxial crystal symmetry, one defines the permittivity tensor as given in equation 2.2

$$\bar{\epsilon} = \begin{pmatrix} \epsilon_{xx} & 0 & 0 \\ 0 & \epsilon_{yy} & 0 \\ 0 & 0 & \epsilon_{zz} \end{pmatrix} \tag{2.2}$$

ϵ_{xx} and ϵ_{yy} represent the permittivity for waves propagating in the direction planar to the material interface. A uniaxial medium has a planar symmetry such that $\epsilon_{xx} = \epsilon_{yy}$ and thus we can define $\epsilon_{\parallel}$ to be the planar permittivity in the xy-plane. Subsequently, we can define the permittivity in the direction normal to the interface (ϵ_{zz}) with the perpendicular permittivity $\epsilon_{\perp}$.

Equation 2.1 supports time harmonic plane wave solutions of the form $\tilde{A}e^{i(\vec{k}\cdot\vec{r}-\omega t)}$ if the following dispersion relation given in equation 2.3 is satisfied:

$$\vec{k} \times (\vec{k} \times \vec{E}) = \left(\frac{\omega}{c}\right)^2 \bar{\epsilon}\vec{E} = k_0^2 \bar{\epsilon}\vec{E} \tag{2.3}$$

$\vec{k}$ is the wavevector, ω is the angular frequency and $\vec{E}$ is the electric field. If we now express equation 2.3 in matrix form we arrive at the following:

$$\begin{pmatrix} \epsilon_{\parallel}k_0^2 - k_y^2 - k_z^2 & k_x k_y & k_x k_z \\ k_x k_y & \epsilon_{\parallel}k_0^2 - k_x^2 - k_z^2 & k_y k_z \\ k_x k_z & k_y k_z & \epsilon_{\perp}k_0^2 - k_x^2 - k_y^2 \end{pmatrix} \begin{pmatrix} E_x \\ E_y \\ E_z \end{pmatrix} = 0 \tag{2.4}$$

For non-trivial solutions to equation 2.4 for E_x, E_y and E_z, we must equate the determinant of the left matrix to 0. This gives the allowed states of the k_x, k_y and k_z forming a wavevector surface for a given frequency. This is often referred to as the isofrequency surface or the dispersion relation for the material.

Here, we can have either the electric field, $\vec{E}$, be parallel to the interface (TE polarization) or the magnetic field, $\vec{B}$, be parallel to the interface (TM polarization). Considering TE polarization, where $E_z = 0$, from equation 2.3 we can determine that the dispersion relation is equivalent to that of an isotropic medium with permittivity $\epsilon_{\parallel}$, such that $\epsilon_{\parallel}k_0^2 - (k_x^2 - k_y^2 - k_z^2) = 0$. This is the dispersion for ordinary waves in a uniaxial medium. If we now look at the case for TM polarization, where $B_z = 0$, and using $\nabla \times \vec{B} = \frac{1}{c}\frac{\partial(\vec{\epsilon}\vec{E})}{\partial t}$ from maxwell's equations we now see that equation 2.3 gives the following dispersion:

$$k_0^2 - \left(\frac{k_x^2 + k_y^2}{\epsilon_{\perp}} + \frac{k_z^2}{\epsilon_{\parallel}}\right) = 0 \tag{2.5}$$

Equation 2.5 is the dispersion relation for extraordinary waves in a conventional uniaxial medium. The isofrequency surface for this dispersion can be seen in figure 2.1(a). In section 2.2 we will see how hyperbolic dispersion can be achieved by tuning the permittivites of a uniaxial crystal.

2.2 Hyperbolic Dispersion

Hyperbolic Metamaterials (HMMs) are artificial uniaxial materials with an extremely anisotropic dielectric tensor. The extreme anisotropy is characterized by requiring the components of the permittivity to be defined such that $\epsilon_{xx} = \epsilon_{yy}$ and $\epsilon_{zz} \times \epsilon_{xx} < 0$. The physical meaning of the anisotropy is that the material is behaving like a metal in one direction ($\Re(\epsilon) < 0$) and like a transparent dielectric in the other ($\Re(\epsilon) > 0$). This type of extreme anisotropy is not seen at all ranges of the electromagnetic spectrum and thus must be engineered with nanostructured metamaterials.

If we now incorporate this extreme anisotropic behaviour into the dispersion for extraordinary waves in a uniaxial medium (equation 2.5), we note that the isofrequency surface is now a hyperboloid. The hyperbolic dispersion of the isofrequency surface is a result of the extreme anisotropy of the HMM. This is in contrast to the spherical or ellipsoidal isofrequency surfaces seen in conventional materials.

This hyperbolic behaviour of the isofrequency surface can be defined for two separate regimes, giving rise to two types of HMMs. Type I HMMs have a single negative component of the dielectric tensor in a direction normal to the metamaterial surface ($\epsilon_{zz} = \epsilon_{\perp} < 0$) whereas Type II HMMs have two negative components of the uniaxial dielectric tensor that are planar to the metamaterial surface $\big(\epsilon_{xx} = \epsilon_{\parallel} < 0, \epsilon_{yy} = \epsilon_{\parallel} < 0\big)$. This is shown in figure 2.1(b) and figure 2.1(c) respectively.

The unbounded hyperboloid isofrequency surfaces, seen in figure 2.1(b) and figure 2.1(c), display the ability of the Type I and Type II HMMs to support waves with large wavevectors (high-k waves) much larger than the free space wavevector ($k_0 = \frac{\omega}{c}$). These high-k waves are normally evanescent in conventional media with bounded (spherical or ellipsoidal) isofrequency surfaces. However, the high-k waves have the ability to propagate in the HMM as a result of its characteristic hyperbolic dispersion [4, 5, 7]. The origin and unique properties of such high-k waves is discussed in section 2.4. The necessary building blocks for creating metamaterials with this hyperbolic dispersion is discussed in section 2.3.1.

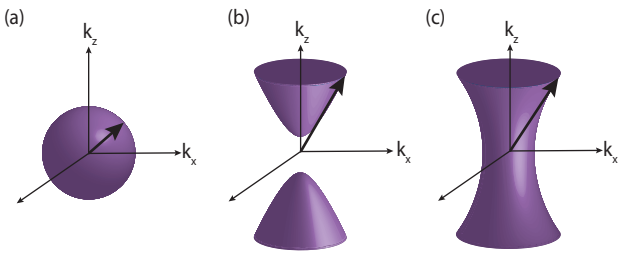

Figure 2.1: k-space topology. (a) Spherical isofrequency surface for an isotropic dielectric. (b) Hyperboloid isofrequency surface for a uniaxial medium with an extremely anistropic dielectric response (Type I HMM: $\epsilon_{zz} < 0, \epsilon_{xx}, \epsilon_{yy} > 0$) (c) Hyperboloid isofrequency surface for an extremely anistropic uniaxial medium with two negative components of the dielectric tensor (Type II HMM: $\epsilon_{xx}, \epsilon_{yy} < 0, \epsilon_{zz} > 0$). The (b) Type I and (c) Type II metamaterials can support waves with infinitely large wavevectors in the effective medium limit. Such waves are evanescent and decay away exponentially in vacuum.

2.3 Building Blocks of a Hyperbolic Metamaterial

2.3.1 Practical Realizations

There are two main methods for engineering materials with the characteristic hyperbolic dispersion. One realization of an HMM involves a planar multilayer structure with alternating subwavelength metal-dielectric layers [4, 5, 13]. The second structure involves embedding metallic nanorods in a dielectric host [2, 14, 15, 16, 17, 18]. A schematic of both of these realizations can be seen in figure 2.2(b) and figure 2.2(c) respectively. The multilayer and nanorod design, according to effective medium theory (section 2.3.2), give rise to the extreme anisotropy required to achieve the hyperbolic dispersion.

2.3.2 Effective Medium Theory: Multilayer Structures

Operation with layers much smaller than the interacting wavelength allows for the use of Effective Medium Theory (EMT) to model the optical response of a multilayer structure. The medium can be characterized as an effective medium as the magnitude of the fields do not change significantly across the thickness of the slab. The permittivity of both the parallel ($\epsilon_{\|}$) and perpendicular ($\epsilon_{\perp}$) components of the dielectric tensor can be determined by assuming an averaged displacement field and applying the electromagnetic boundary conditions:

$$\epsilon_{\|} = \epsilon_2 \rho + (1-\rho)\epsilon_1 \tag{2.6}$$

$$\frac{1}{\epsilon_{\perp}} = \frac{\rho}{\epsilon_2} + \frac{1-\rho}{\epsilon_1} \tag{2.7}$$

$$\epsilon_{eff} = \begin{pmatrix} \epsilon_{\parallel} & 0 & 0 \\ 0 & \epsilon_{\parallel} & 0 \\ 0 & 0 & \epsilon_{\perp} \end{pmatrix} \tag{2.8}$$

Here ϵ_1 and ϵ_2 represent the permittivities of the two different alternating layers of a multilayer structure and ϵ_{eff} is the effective dielectric tensor of the uniaxial slab. For the case of a semiconductor HMM we consider $\epsilon_1 > 0$ (dielectric)and $\epsilon_2 < 0$ (metallic) in order to achieve the hyperbolic dispersion for the structure [4, 5]. The fill fraction, $\rho = d_2/(d_1+d_2)$, is the weighted fraction of the thickness of layer 2 (d_2) to the total thicknesses of layer 1 (d_1) and layer 2 of the multilayer structure.

It is important to realize that homogenization using effective medium theory is only valid and comparable to a practical structure when the wavelength of the incoming radiation is much larger than the unit cell size of the metamaterial. EMT predicts the presence of unique short wavelength high-k states in the metamaterial (section 2.4) and it is important to compare these results with that of a practical metamaterial structure. We will show that factors such as type of materials used, doping levels, material fill fractions, and unit cell size all effect the resulting EMT and practical structure response of the HMM media. Specifically, all of these parameters effect the dispersion of the high-k states within the HMM as is discussed in section 2.4.

2.3.3 Mid-IR Hyperbolic Metamaterials

A variety of different materials can be used to create HMM structures depending on the operating region of the EM spectrum. Figure 2.2 shows some of the possible materials. The main consideration when creating HMM structures is the material with metallic character and the frequency of its plasmonic response as well as its filling fraction. Silver has proven to be the best choice of metal in the visible region due to its relatively lower optical losses (absorption). However, at longer wavelengths (eg: near-infrared and mid-infrared) it becomes increasingly reflective leading to large impedance mismatches with other known materials. Alternative materials, such as transparent conducting oxides and transition metal nitrides [19, 20] can exhibit metallic behaviour in the near-IR. Additionally, highly doped III-V semiconductors [13] can also have metallic responses in the mid-IR.

Silver and gold exhibit plasma frequencies in the UV and as a result are extremely reflective in the infrared. If one wants to create metamaterials with hyperbolic dispersion in the mid-IR, materials with lower energy plasma frequencies, such as semiconductors, need to be incorporated into the metamaterial design. Fabricating mid-IR hyperbolic metamaterials with semiconductors also creates the unique ability to observe quantum confinement effects such as embedded quantum wells in the system which are not possible with metals and dielectrics. This allows for

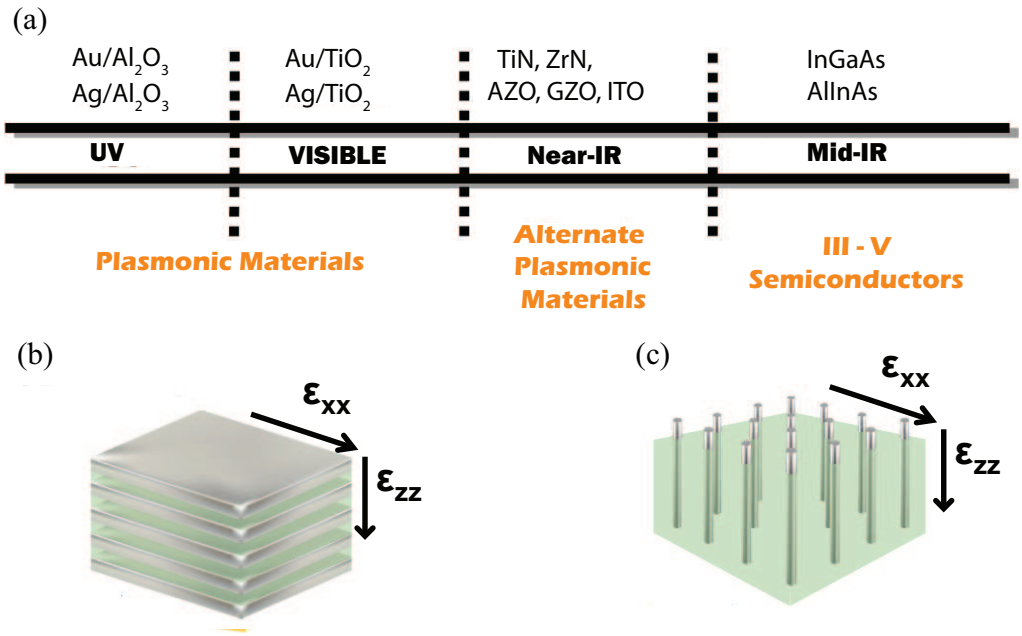

Figure 2.2: (a) Materials used to create hyperbolic metamaterials depending on region of operation in the electromagnetic spectrum (UV to mid-IR frequencies) (b) Multilayer structure consisting of alternating metallic and dielectric layers forming a metal-dielectric superlattice. (c) Nanowire structure consisting of metallic nanorods embedded in a dielectric host. In both (b) and (c) the constituent components are subwavelength allowing characterization with effective medium theory [6].

the possibility of incorporating active components into the HMM creating novel quantum mechanical effects in the structure.

Compound or III-V semiconductors are used widely in optoelectronic devices such as LEDs, semiconductor lasers, and infrared detectors. III-V semiconductors, as their name suggests, are composite semiconductor structures made from group III semiconductor elements (eg. boron, aluminum, gallium, indium) and group V semiconductor elements (eg. nitrogen, phosphorous, arsenic). The direct bandgap nature and tunability of III-V semiconductors have proven useful for semiconductor optoelectronic devices [13, 21].

The flexiblity of doping compound semiconductors makes it easier to tune and modify their plasma frequencies. This makes them useful for creating multilayer semiconductor hyperbolic metamaterials, as one can alternate "dielectric" and "metallic" semiconductor layers to provide the hyperbolic dispersion for the structure. Furthermore, one can more easily fabricate these multilayer structures by taking advantage of the mature fabrication processes developed for industrial semiconductors. Chapter 3 looks at creating these novel semiconductor HMMs as well as harnessing their quantum confinement properties to introduce new quantum effects not

previously seen with other hyperbolic metamaterial structures.

2.4 The Modes of a Hyperbolic Metamaterial

In this section we discuss the plasmonic origin of the high-k modes of the hyperbolic metamaterial. We will start by discussing the plasmonic modes of a thin metal film and then move on to metal-dielectric multilayer structures.

2.4.1 Thin Metal Film

Metals interact with electromagnetic radiation through the motion of their free electrons. In the optical regime, incoming radiation has a high enough frequency to create resonant charge density fluctuations of the free electrons in the metal. These charge oscillations are known as plasmons and can manifest in the metal as either volume oscillations or surface oscillations.

Surface plasmons, which exist at the interface between a metal and dielectric, are strongly confined to the surface of the metal and have characteristically large optical fields. Surface plasmon polaritons (SPPs) are surface charge density oscillations that propagate along this metal-dielectric interface. The SPP is a surface bound mode whose fields exponentially decay in the direction perpendicular to the interface and is a solution to the wave equation. Applying Maxwell's equations and the electromagnetic boundary conditions for TM polarized light, one can derive the SPP dispersion relation for a metal-dielectric halfspace as given in equation 2.9 and equation 2.10 respectively.

$$k_{x,spp}^2 = \frac{\epsilon_1 \epsilon_2}{\epsilon_1 + \epsilon_2} \frac{\omega^2}{c^2} \tag{2.9}$$

$$k_{z1,z2,spp}^2 = \frac{\epsilon_{1,2}^2}{\epsilon_1 + \epsilon_2} \frac{\omega^2}{c^2} \tag{2.10}$$

$k_{x,spp}$ and $k_{z,spp}$ are the planar and perpendicular wavevector components of the surface plasmon polariton respectively. Here, ϵ_1 is the permittivity of the metal and ϵ_2 is the permittivity of the dielectric. As stated earlier, the SPP is a bound surface mode with exponentially decaying tails away from the interface. This requires the perpendicular wavevector component given in equation 2.10 to be purely imaginary. In order to fulfill this requirement, one can see that we have the following necessary conditions for an SPP mode between a metal-dielectric halfspace: $\epsilon_1 \epsilon_2 < 0$ and $\epsilon_1 + \epsilon_2 < 0$. Specifically, in order to support an SPP we require a negative permittivity material (such as a metal) whose absolute value of the permittivity is greater than that of the other dielectric.

Surface plasmon polaritons, in practical realizations, can be excited on thin

metal films. A metal (eg. silver) sandwiched between two dielectrics (e.g. air) will support SPPs on both the top and the bottom interface. If the metal is thin enough, such that the tails of the SPP do not decay away completely in the direction perpendicular to the interface, the two SPPs can couple with each other, resulting in mode hybridazation. If the two dielectrics sandwiching the metal are identical, this leads to the formation of even and odd modes of the SPP.

The surface plasmon polariton solutions arise from the wave equation in which there are no driving terms, as was shown earlier for the two infinite half spaces. We can similarily obtain the solutions for SPPs in a coupled system using the set of electromagnetic boundary conditions by looking at the expression for the reflection coefficient for TM polarized light from a slab of material, as given in equation 2.11 [22].

$$r_{TM} = \frac{r_{12} + r_{23}e^{2idk_{z2}}}{1 + r_{12}r_{23}e^{2idk_{z2}}} \tag{2.11}$$

r_{12} and r_{23} are the TM reflection coefficients from the top and bottom of the metal surface respectively and k_{z2} is the perpendicular wavevector component in the metal. Here, we can find the modes of this system by finding the poles of equation 2.11. This results in two solutions for a metal sandwiched between two identical dielectrics which are the even and the odd SPP. Figure 2.3 shows the hybridized SPP modes for thin 30 nm silver film sandwiched between two dielectric halfspaces.

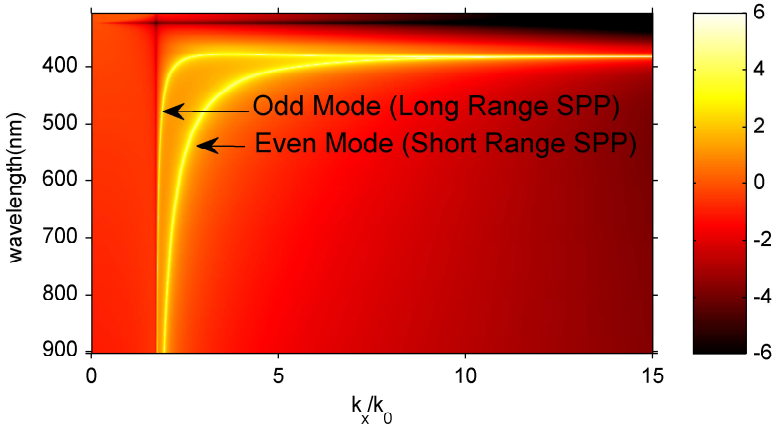

Figure 2.3: Transmission (log scale) through a 30 nm low loss silver layer sandwiched between two dielectric halfspaces using the transfer matrix method. The near field coupling between the SPP at the top and bottom metal interfaces results in mode hybridization creating the even (short range SPP) and odd (long range SPP) modes. k_x is in the in-plane wavevector and k_0 is the free space wavevector.

Odd SPP modes have long propagation distances as their fields are pushed out of the metal and are less subject to the larger metallic losses. Odd modes are

therefore referred to as long-range SPPs as their propagation length increases with decreasing metal thickness. Conversely, even modes are short-range SPPs as their fields are more confined to the metal. For short-range SPPs the confinement to the metal increases as the metal thickness decreases limiting the SPP's propagation length. We will see that increasing the number of metal-dielectric layers leads to an increasing number of coupled even and odd SPP modes which are the origin of the high-k states in multilayer HMM structures (section 2.4.2).

2.4.2 High-k Modes of a Multilayer Hyperbolic Metamaterial

Section 2.3.1 showed the possibility of creating a planar hyperbolic metamaterial structure with alternating subwavelength metal-dielectric layers, creating a metal-dielectric superlattice. Additionally, in section 2.4.1 we saw that surface plasmon polaritons can be supported at metal-dielectric interfaces. Multiple SPPs can be excited simultaneously at each of the metal dielectric interfaces in the multilayer structure. The SPPs at each interface can then couple together through the interaction of their near-fields. As a result, much like we saw mode hybridization leading to the creation of even and odd SPP modes in section 2.4.1, we see similar multiple SPP hybridizations in a multilayer structure.

Figure 2.4 shows the transmission spectra through an idealized low loss 200 nm thick $silver - TiO_2$ multilayer hyperbolic metamaterial using the transfer matrix method and effective medium theory. We can see a series of bright bands appearing

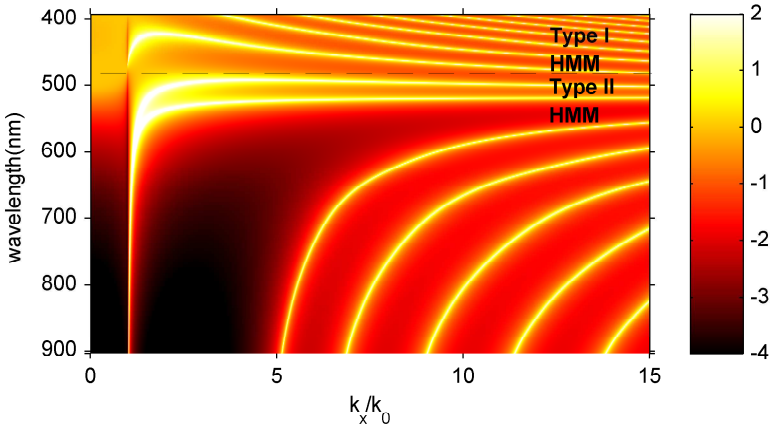

Figure 2.4: Transmission (log scale) through a 200 nm homogenized $silver - TiO_2$ hyperbolic metamaterial using the transfer matrix method. The bright bands in the Type I and Type II HMM regions represent the high-k modes which are the bloch waveguide modes of the structure. Idealized silver and TiO_2 layers are used to clearly show the effects. k_x is the in-plane wavevector and k_0 is the free space wavevector.

in the transmission spectra at large values of the in-plane wavevector (k_x). In the idealized half-space limit, these bands would correspond to the continuum of high-k states of a hyperbolic material. However, due to the finite size of the structure, the continuum of high-k states manifest as a series of bright bands that are in actuality the bloch waveguide modes of the metal-dielectric superlattice (figure 2.4). These are, in fact, the modes that arise from the near-field coupling of the SPPs at each metal-dielectric interface within the structure.

One notes that the HMM modes exist at large values of the in-plane wavevector (k_x) as a result of the light-matter coupling. These modes, normally evanescent in vacuum and conventional materials, propagate in the HMM structure. The existence of these unique high-k modes in the HMM creates a large photonic density of states (section 2.4.3)) with many potential applications [6, 8, 23].

2.4.3 The Photonic Density of States

The spontaneous emission lifetime of an emitter can be controlled by engineering the optical environment that surrounds it. This is due to the fact that the environment has a certain photonic density of states (PDOS) available that can couple with the emitter. If the number of available photonic states increases (decreases) the spontaneous decay rate (Γ_r) of an emitter is enhanced (suppressed) as there are more (less) available photonic modes [8, 9]. For example, an emitter placed close to a photonic crystal or microcavity will see a large enhancement to its spontaneous emission decay rate for wavelengths that can couple into the resonant modes of the structure [24, 25, 26, 27]. Specifically, at the resonant modes there is a large enhancement to the PDOS. The enhancement in the radiative decay rate relative to the free space decay rate is known as the Purcell factor. Controlling the rate of emitter spontaneous emission and coupling it into the desired states of a structure is a high area of interest in the field of radiative decay engineering [8, 9, 23, 28, 29].

Hyperbolic Metamaterials have shown promise as a viable tool for radiative decay engineering, especially in the field of quantum nanophotonics [6, 8, 30]. This is due to the large PDOS available in HMMs provided by their ability to support an infinitely large number of high-k states in the ideal limit [4, 30]. For example, an emitter placed close to an HMM will see a large enhancement to its radiative decay rate (Γ_r), due to the large number of additional states it now has available to couple into: $\Gamma_r = \Gamma_{prop} + \Gamma_{plasmon} + \Gamma_{high-k}$. Large Purcell factor enhancements with HMMs were proven both proven both experimentally [9, 23, 31] and numerically [28, 29] by a number of groups.

Photonic crystals and microcavities have also shown Purcell factor enhancements however, unlike HMMs, they are resonant structures and thus have a limited bandwidth where such enhancements are possible. HMMs are able to create a broadband

enhancement to the Purcell factor as a result of the continuum of high-k states unlike their resonant structure counterparts. This could potentially be useful for broad-band single photon sources [8, 32].

Determination of the spontaneous emission decay rate of an emitter can be achieved by calculating the local photonic density of states. The total local density of states (LDOS) can be found from the imaginary component of the dyadic Green's function as given in equation 2.12 for a frequency ω_o at position r_o (appendix A). As outlined in appendix A, we can further define the decay rate of an emitter as a function of the LDOS (Eqation 2.13) where μ is the dipole moment [22, 33]. We will see that this Green's function formalism can be applied to determine the radiative decay enhancement for an emitter placed in the vicinity of an HMM and help us to characterize potential superradiant behaviour between a pair of emitters (section 4.1).

$$\rho(r_0, \omega_0) = \frac{2\omega_o}{\pi c^2} \Im(Tr[\bar{G}(r_0, r_0; \omega_0)]) \tag{2.12}$$

$$\Gamma = \frac{2\omega_0}{3\hbar\epsilon_0} |\mu|^2 \rho_\mu(r_0, \omega_0) \tag{2.13}$$

Chapter 3

Strong Coupling in Semiconductor HMMs

A majority of work in the field of hyperbolic metamaterials has dealt exclusively with the optical regime of the electromagnetic spectrum. In this chapter, we propose and analyze an active multilayer semiconductor structure able to achieve hyperbolic dispersion in the mid-IR. Multilayer semiconductor structures can create a series of quantum wells with transition energies at mid-IR frequencies which can potentially behave as active components within an HMM.

The interaction of the subwavelength modes with the transition resonances of quantum wells can also lead to new coherent effects not previously seen in HMM structures. We show that new mixed polaritonic states are created in the system due to strong coupling between high-k modes of an HMM and the intersubband transitions (ISBTs) of the embedded quantum wells. In this chapter, we discuss the origin of such strong coupling behaviour (section 3.1) as well as its manifestation in semiconductor HMM structures in both the effective medium approach (section 3.4) as well as a practical multilayer structure (section 3.5).

In this thesis we present the first work to show strong coupling in hyperbolic metamaterials. This work paves the way for future research on quantum strong coupling with hyperbolic metamaterial structures.

3.1 Strong Coupling

Strong coupling has been a key area of interest over the past decade for its potential in creating coherent and entangled states between light and matter [34, 35, 36, 37, 38]. It is best understood by first discussing the nature of the weak coupling regime. We focus our arguments particularly to metallic structures instead of dielectric photonic cavities. If a single emitter is placed in the near field above a metal surrounded

by air, it can weakly couple by emitting photons into a surface plasmon polariton mode at the metal-dielectric interface (figure 3.1). The SPP will then propagate along this interface until it is absorbed by the metal [22]. Weak coupling, therefore, is an example of an irreversible spontaneous emission process. The field of hyperbolic metamaterials has dealt almost exclusively in this weak coupling regime whereas strong coupling behaviour with surface plasmons has been shown previously [39]. The work, as described in section 2.4.3, has primarily dealt with enhancing the Purcell factor by weak coupling the emitter to the continuum of high-k states in the HMM.

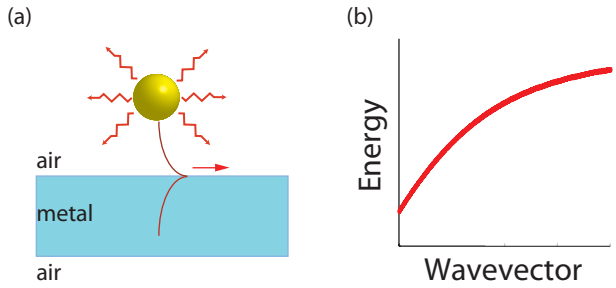

Figure 3.1: (a) Single emitter weak coupling into the surface plasmon polariton at a metal dielectric interface. (b) Arbitrary dispersion of an emitter weakly coupled into a surface plasmon polariton propagating along the surface of a metal. (a) and (b) show an irreversible spontaneous emission process.

Strong coupling, unlike the weak coupling limit, relies on the back-action between the emitter and its environment. Multiple groups have studied a single emitter within a cavity to create the large interaction required for a strong coupling process (figure 3.2(a)) [34]. Specifically, strong coupling will be achieved if the coupling strength between the modes ($g_{coupling}$) is greater than the sum of the radiative broadening of the emitter ($\gamma_{transition}$) and the loss of the cavity mode (γ_{cavity}) (equation 3.1). This results in a mixed polaritonic state in the dispersion (figure 3.2(b)) with a characteristic anti-crossing indicative of strong coupling behaviour. The upper and lower branches of the dispersion are then separated by the quantum mechanical vacuum rabi splitting energy. The back action between the emitter and the environment results in this mixed state that oscillates between the two modes of the system.

$$g_{coupling} > \gamma_{transition} + \gamma_{cavity} \tag{3.1}$$

Incorporating strong coupling phenomena into HMMs could lead to novel mixed and coherent states not previously seen in such structures. Studies in the field of strong coupling have dealt primarily with single emitters interacting with larger

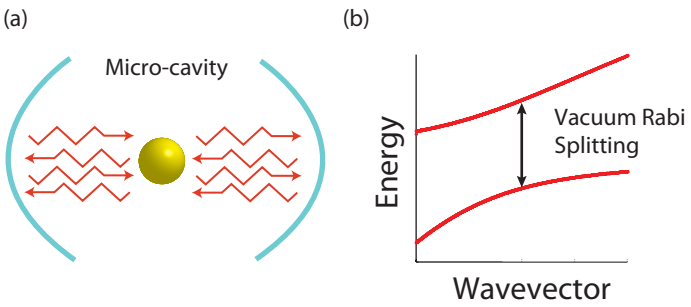

Figure 3.2: (a) Single emitter placed within a micro-cavity strongly coupled to a cavity mode. The strong interaction leads to a back action between the emitter and its environment. (b) Arbitrary polaritonic dispersion of an emitter strongly coupled to a cavity mode. The characteristic anti-crossing results in an upper and lower branch to the polariton which are separated by the vacuum rabi splitting energy. (a) and (b) show a reversible spontaneous emission process.

structures such as micro-cavities or photonic crystals ([34]). Multilayer HMMs, however, require different design considerations for strong coupling implementation primarily because it is not a cavity or resonant structure. Also, the major advantage of HMMs lies in their ability to support subwavelength modes increasing their interactions with emitters. However, HMMs are also lossy structures due to their partial metallic composition. Thus, in order to see strong coupling in HMMs, we will require a large number of emitters that can be embedded within the system in order to create the large degree of interaction necessary to mitigate the losses in the system. We will see that one possible method is through the use of embedded multiple quantum wells in a semiconductor HMM structure as described in section 3.2.

3.2 Semiconductor Hyperbolic Metamaterials

3.2.1 Introduction

The building blocks of HMMs can be composed of metals such as silver and gold that exhibit plasmonic resonances near their plasma frequency in the UV. The high plasma frequency of these metals makes them very reflective in the infrared. Semiconductors, however, allow for the ability to harness plasmonic resonances in the mid-IR [13]. Specifically, we can use a degenerately doped semiconductor as the metallic component in the hyperbolic metamaterial. The large number of free carriers make it behave very close to a drude metal with a plasma frequency in the infrared [13]. These semiconductor HMMs, aside from their ability to support high-k states in the NIR and mid-IR, have the distinct advantage of tunable plasma

frequencies through the variation of their electron doping density. This results in an increased control of the dispersion of the semiconductor's permittivity, subsequently providing the ability to create the extreme anisotropy of a structure necessary to achieve hyperbolic dispersion.

We propose a planar semiconductor HMM composed of alternating layers of a multiple quantum well (MQW) slab (dielectric component) and a degenerately doped semiconductor (metallic component) with the ability to support high-k waves in the infrared (figure 3.3(a)). The MQW slab is composed of layered semiconductors to create a series of quantum wells. It is shown that the high-k waves of the semiconductor HMM strong couple to intersubband transitions (ISBTs) present in the MQW slab as a result of quantum confinement effects. These active semiconductor HMMs can find potential use in quantum well infrared photodetectors and tunable intersubband light-emitting devices [21]. We emphasize that the proposed semiconductor super-lattice structure can be fabricated by lattice matched molecular beam epitaxy [13].

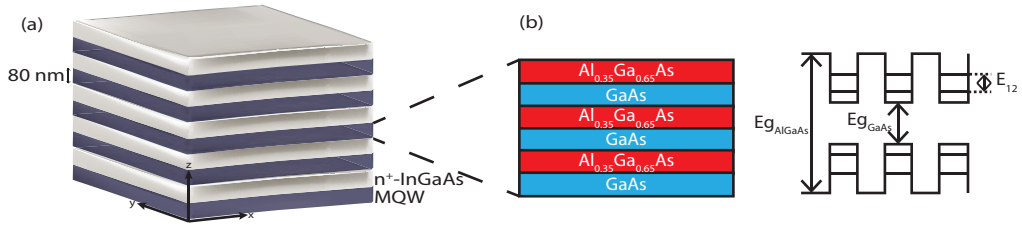

Figure 3.3: (a) Multilayer realization of a semiconductor HMM. The structure consists of alternating 80 nm thick subwavelength layers of a dielectric MQW slab and degenerately doped n^+-InGaAs. The extreme anisotropy of the structure results in a hyperbolic isofrequency surface. (b) Quantum well structure of the MQW slab (idealized).

3.2.2 Dielectric Component: Multiple Quantum Well Slab

We now analyze the semiconductor HMM with an active dielectric layer in the form of a MQW slab. The important aspect to note is that the MQW slab itself is modeled with an EMT approach. Previous analytic and experimental work have shown the validity of using EMT to model the MQWs within the structure [21, 40]. The QW thickness, L_{QW} (6 nm), and the MQW period, L_{MQW} (20 nm), are much smaller than the wavelength of the incident infrared radiation and the wells themselves are assumed to be quantum mechanically isolated from each other. The MQW slab is composed of alternating subwavelength layers of $Al_{0.35}Ga_{0.65}As$ and GaAs to form the multiple quantum wells, where $Al_{0.35}Ga_{0.65}As$, with its larger bandgap relative to GaAs, creates the barriers for the structure (figure 3.3(b)). Note that

figure 3.3(b) shows an idealized quantum well structure as band discontinuities at the $Al_{0.35}Ga_{0.65}As$ and GaAs heterojunction are not shown. This fact does not significantly effect the analysis done in this thesis.

MQWs show free electron movement in the plane parallel to the surface (the x-y plane) and quantum confinement, with possible ISBTs, in the the plane normal to the interface (z-direction) (figure 3.3). This quasi-two-dimensional electron gas can be modeled with an anisotropic dielectric tensor similar to other uniaxial media. The permittivity of the MQW slab, in the plane parallel to the interface, is effectively characterized by a Drude model [21, 41]:

$$\epsilon_{xx}^{d} = \epsilon_{yy}^{d} = \epsilon_{y} - \frac{\omega_{p,mqw}^{2}}{\omega^{2} + i\omega\gamma_{1}} \tag{3.2}$$

Permittivity in the plane perpendicular to the MQW interface is characterized with a Lorentzian Oscillator Model in order to incorporate the quantum confinement effects of the structure, specifically the resonance at the ISBT energy [21, 41]:

$$\frac{1}{\epsilon_{zz}^{d}} = \frac{1}{\epsilon_{z}} - \frac{\frac{\omega_{p,mqw}^{2} f_{12}}{2\omega\gamma_{2}\epsilon_{well}}}{\frac{E_{12}^{2} - \hbar^{2}\omega^{2}}{2\hbar^{2}\gamma_{2}\omega} - i} \tag{3.3}$$

Here, ϵ_y and ϵ_z represent the mean effective background dielectric constant and are given as $\epsilon_y = (1 - L_{QW}/L_{MQW})\epsilon_{barrier}$ and $\epsilon_z^{-1} = (1 - L_{QW}/L_{MQW})/\epsilon_{barrier} + (L_{QW}/L_{MQW})/\epsilon_{well}$ [41], with $\epsilon_{barrier}$ (9.88) and ϵ_{well}(10.36) representing the undoped background dielectric constant for the barrier and well respectively. $\omega_{p,mqw} = (n_s e^2/m\epsilon_0 L_{MQW})^{1/2}$ is the plasma frequency for the system where e is the elementary charge of the electron, ϵ_0 is the vacuum permittivity constant, m* = 0.0665m is the effective mass of the electron, where m is the mass of an electron in vacuum, and $n_s = 1.5 \times 10^{12} cm^{-2}$ is the areal electron density per quantum well. f_{12} corresponds to the oscillator strength of the resonance which depends on the transition energy of the ISBT, the effective mass of the electron and the intersubband dipole matrix element. E_{12} is the ISBT transition energy, which, for the parameters established is set to be equal to $\lambda_{ISBT} = 5\mu$m (0.2480 eV). $\gamma_1 = \gamma_2$ is the electron scattering rate given as $7.596 \times 10^{12} s^{-1}$ [21].

The superscript d in the definitions of both the parallel and perpendicular permittivities given in equation 3.2 and equation 3.3 respectively, is used to emphasize that the MQW slab is purely dielectric as we are operating above the plasma frequency ($\omega_{p,mqw}$) of the MQW slab. The dispersion for the MQW slab can be seen in figure 3.4(a).

One will note that the properties of the ISBT are only present in the perpendicular (ϵ_{zz}) component of the dielectric tensor (equation 3.3) as the ISBT can only be excited with electric fields polarized in the growth direction (z-direction) of the

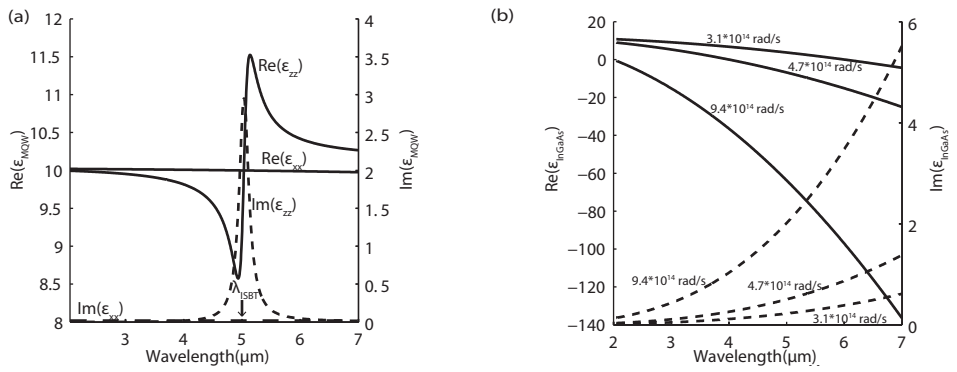

Figure 3.4: (a) Perpendicular and parallel permittivities of the purely dielectric MQW slab. The resonance at a wavelength of $\lambda_{ISBT} = 5\mu$m corresponds to the energy of the intersubband transition in a single quantum well of the MQW structure. (b) Dispersion of the n^+-InGaAs semiconductor layer at different plasma frequencies. The negative permittivity of the InGaAs layer (metallic response) is required in order to realize a hyperbolic dispersion in the semiconductor HMM.

slab. This is due to the fact that wavefunctions of each subband are also bound in the z-direction and thus, due to orthogonality conditions, transitions between states require absorption from z-polarized E-fields. S-polarized light will have no z-component of the electric field and so p-polarized incidence is required to see effects of the ISBTs in the semiconductor HMM. Note that the ISBT resonance is compatible with the high-k modes of the metamaterials since both occur only for p-polarized light.

3.2.3 Metallic Component: Degenerately Doped InGaAs Layer

The MQW slab presented in section 3.2.2 is purely dielectric such that $\Re(\epsilon^d_{xx}) > 0$ and $\Re(\epsilon^d_{zz}) > 0$. A separate metallic layer is needed to achieve hyperbolic dispersion in a super-lattice geometry as outlined in section 2.2. The plasmonic metal in this case can be a degenerately doped n^+-InGaAs semiconductor with $\Re(\epsilon_{InGaAs}) < 0$. The n^+-InGaAs layer is assumed to be isotropic and approximated with Drude-like behaviour [13]:

$$\epsilon_{InGaAs} = \epsilon_{b,InGaAs}\left(1 - \frac{\omega^2_{p,InGaAs}}{\omega^2 + i\omega\gamma}\right) \tag{3.4}$$

Here, $\epsilon_{b,InGaAs}$ is the background dielectric set at 12.15, γ is the electron scattering rate set to $1 \times 10^{13} s^{-1}$ and $\omega_{p,InGaAs}$ is the plasma frequency. Figure 3.4(b) shows the dispersion of ϵ_{InGaAs} at different plasma frequencies of the semiconductor. For the analysis in this paper, we set $\omega_{p,InGaAs} = 9.43 \times 10^{14} rad/s$ to best interact with the MQW slab. For experimental considerations, operation at lower InGaAs

plasma frequencies would need to be considered and, as a result, the MQW slab's quantum well thickness and period would also need to be adjusted such as to tune the ISBT energy to best interact with the modes of the structure.

3.3 Strong Coupling in Semiconductor Hyperbolic Metamaterials

3.3.1 Semi-classical Perspective

In the previous section we presented the semiconductor based active dielectric layer and metallic layer needed for achieving multilayer hyperbolic metamaterials. Before we present the characteristics of strong electromagnetic interactions in this active metamaterial, we discuss the semiclassical theory of strong coupling for the case of hyperbolic media.

Strong coupling is the result of large interaction two distinct resonances within a system as outlined in section 3.1. In a semiconductor HMM, for example, strong light-matter coupling is possible between the dispersionless resonance of the ISBTs and the high-k modes of the structure. Strong coupling between two resonances results in a typical polaritonic dispersion in the domain of interaction such that the entire excitation is treated as one entity unlike the weak coupling limit [42]. Specifically, in the strong coupling regime, the strength of coupling between the two resonances is greater than the sum of the damping rates of both resonators. We will first observe how to semi-classically derive strong coupling behaviour between a dispersionless resonance, such as an ISBT, and a high-k mode of an HMM. We can then extend this analysis to our understanding of the strong coupling interaction as described in section 3.3.2.

Using the dispersion outlined in equation 2.5 we define the energy for a high-k mode in a low loss semiconductor HMM as:

$$E^2_{high-k}(q) = \hbar^2 c^2 \left(\frac{q^2}{\epsilon_{zz}} + \frac{k_z^2}{\epsilon_{xx}} \right) \tag{3.5}$$

Here $q^2 = k_x^2 + k_y^2$, ϵ_{zz} and ϵ_{xx} are the perpendicular and parallel permittivity respectively, and k_z is the wavevector normal to the interface. It is now assumed that a dispersionless ISBT resonance is added to the HMM in the form of a low loss Lorentzian Oscillator model [40] and, as such, the dispersion given in equation 3.5 can now be rewritten as follows:

$$\left(\frac{\hbar^2 c^2 q^2}{E^2 - \frac{\hbar^2 c^2 k_z^2}{\epsilon_{xx}}} \right) = \epsilon_{zz} + \frac{C}{E^2_{ISBT} - E^2} \tag{3.6}$$

Note that we are only adding the ISBT resonance to the perpendicular (ϵ_{zz}) component of the permittivity as only the perpendicular component will interact with the quantum confinement effects of the HMM (section 3.2.2). C is the constant representative of the oscillator strength of the resonance and E_{ISBT} is the ISBT energy. In the regime of strong coupling, we assume that the resonant energy, E_{ISBT}, and the high-k mode energy, E_{high-k}, become degenerate such that $E{\approx}E_{high-k}{\approx}E_{ISBT}$ [40]. Taking this into account and solving for E to determine the resultant dispersion of the system from equation 3.6 we arrive at the following:

$$E_{U,L}(q) = \frac{E_{high-k}(q) + E_{ISBT}}{2} \pm \frac{\sqrt{4(\Gamma)^2 + (E_{high-k}(q) - E_{ISBT})^2}}{2} \tag{3.7}$$

Equation 3.7 shows the formation of the resultant upper and lower polariton branches of the dispersion in the regime of strong coupling. The magnitude of the splitting between the upper and lower branches of the dispersion is proportional to $\Gamma^2 = \frac{C\hbar^2c^2q^2}{4\epsilon_{zz}^2 E_{ISBT} E_{high-k}}$ and is much larger than the ISBT linewidth if the resonances are strongly coupled. The polaritonic dispersion emphasizes the mixing of the states between the two resonances as a result of the strong coupling interactions.

3.3.2 Vacuum Rabi Splitting in Semiconductor HMMs

Here we define the strong coupling behaviour in the semiconductor HMM through the vacuum rabi splitting (VRS) energy. The VRS energy denotes the energy level splitting between two coupled resonances within a system and characterizes the degree of strong coupling between them. The semiconductor HMM displays strong coupling phenomena when the energy of the ISBT and the high-k mode become degenerate [43]. The explicit regime of strong coupling occurs when the magnitude of the VRS energy is greater than the sum of the damping of the high-k mode and the radiative broadening of the ISBT resonance [44, 45, 46]. This results in a mixed state between the two resonances of the system leading to a high-k-ISBT polariton.

The resultant dispersion and, more importantly, the magnitude of the splitting energy of the high-k-ISBT polariton can be ascertained by describing the coupling between two oscillators with a 2×2 matrix Hamiltonian given by [45, 46]:

$$H = \begin{pmatrix} E_{ISBT} & \frac{\hbar\Omega}{2} \\ \frac{\hbar\Omega}{2} & E_{high-k} \end{pmatrix} \tag{3.8}$$

Here, E_{ISBT} and E_{high-k} represent the respective energy dispersions of each of the resonances, specifically the ISBT and the high-k mode respectively. For the systems observed here, the ISBT is assumed to be dispersionless and, as such, is at one particular energy across all values of the in-plane wavevector k_x. The coupling matrix term proportional to $\hbar\Omega$ is representative of the vacuum rabi splitting energy

of the system.

We solve the eigenvalue problem for the matrix given in equation 3.8 to determine the dispersion of the system [45, 46]:

$$E_{U,L}(q) = \frac{E_{high-k}(q) + E_{ISBT}}{2} \pm \frac{\sqrt{4(\frac{\hbar\Omega}{2})^2 + (E_{high-k}(q) - E_{ISBT})^2}}{2} \tag{3.9}$$

Here, solutions for the upper and lower branch of the polaritons arise from the strong coupling interaction between the two resonances. Comparing equation 3.7 and equation 3.9, we clearly note that the VRS ($\hbar\Omega$) has taken the place of the semi-classical splitting energy (Γ) in equation 3.7. The splitting energy for the system is now defined with the VRS energy, $\hbar\Omega$. Equation 3.9 assumes that $\hbar\Omega$, is much larger than the radiative broadening of the ISBT, as is the case in the strong coupling regime. For the analysis here, we use equation 3.9, which is analogous to equation 3.7, to determine the semiclassical rabi splitting energy of the semiconductor HMM system. The semiclassical approach is warranted as the system does not deal with single emitters, but a multitude of emitters made present by the many MQW layers. In section 3.4 and section 3.5 we will numerically determine the dispersion of the proposed semiconductor HMM as both an effective medium and a practical structure, respectively, and compare it to the analytical dispersion given by equation 3.9 to determine if strong coupling is present in the system.

3.4 Type II Semiconductor HMMs: Effective Medium Approach

We now analyze the strong coupling interaction between the Type II high-k modes of a semiconductor HMM and the ISBTs of the structure using effective medium theory. As outlined in section 2.3.2, metamaterials interacting with incident radiation at wavelengths much longer than the individual layer thicknesses of the structure can be homogenized and treated as an effective medium.

The semiconductor HMM consists of a series of alternating subwavelength semiconductor based active dielectric and highly doped plasmonic layers. The MQW and InGaAs layers, as shown in figure 3.3(a), are homogenized using EMT for a uniaxial medium (section 3.2.2):

$$\epsilon_{\parallel} = \epsilon_{InGaAs}\rho + (1-\rho)\epsilon_{xx}^{d} \tag{3.10}$$

$$\frac{1}{\epsilon_{\perp}} = \frac{\rho}{\epsilon_{InGaAs}} + \frac{1-\rho}{\epsilon_{zz}^{d}} \tag{3.11}$$

ϵ^d_{xx} and ϵ^d_{zz} are the parallel and perpendicular effective medium permittivities for the MQW slab respectively and ϵ_{InGaAs} is the permittivity of n^+-InGaAs. Note that the permittivities of the MQW slab (ϵ^d_{xx} and ϵ^d_{zz}) are both positive while the InGaAs permittivity (ϵ_{InGaAs}) is negative to achieve the hyperbolic dispersion of the slab. The fill fraction, ρ, is assumed to be 0.5 throughout the analysis as it is assumed that both the MQW and n^+-InGaAs have equal layer thicknesses.

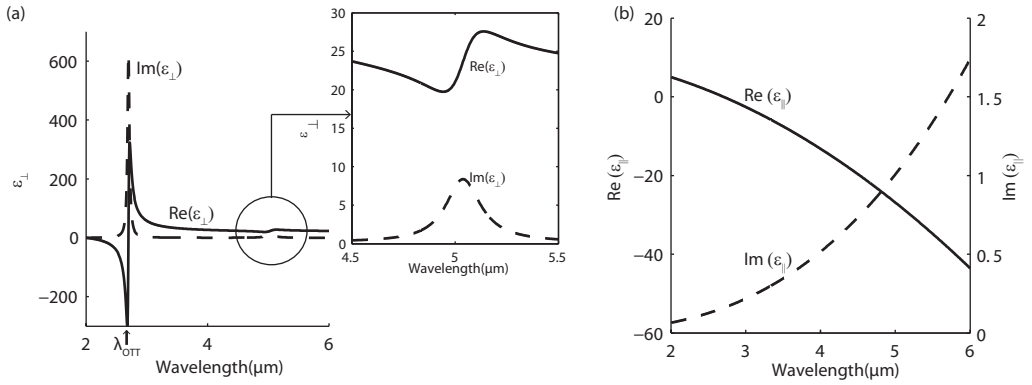

Figure 3.5: (a) Perpendicular and (b) parallel permittivity dispersions for the homogenized MQW-InGaAs structure given by equation 3.10 and equation 3.11 respectively. A clear transition from the Type I to the Type II region is noticed at a wavelength of $\lambda_{OTT} \approx 2.8$ μm where the parallel and perpendicular components of the permittivity both change sign and there is a resulting resonance in the dispersion. A smaller resonance at $\lambda_{ISBT} = 5$ μm is shown in the inset of (a) corresponds to the intersubband transition energy of the structure. In the inset, the imaginary component of $\epsilon_\perp$ is peaked at regions of resonant material absorption due to the ISBT.

The homogenized dispersions shown in figure 3.5 are plotted for wavelengths larger than the plasma frequency and outline the transitions from the Type I region to the Type II region of the HMM. This shift in the dispersion of the metamaterial, where the two-sheeted hyperboloid (Type I) transitions to the single-sheeted hyperboloid (Type II), is known as an optical topological transition (OTT) [31]. In figure 3.5(a) we can see the resonance in the permittivity as result of the topological transition.

The semiconductor HMM is in the Type I region up to $\lambda_{OTT} \approx 2.8$ μm after which point larger wavelengths correspond to a Type II HMM. The small resonance in the perpendicular component of the dielectric constant at λ_{ISBT}=5 μm (inset

figure 3.5(a)) corresponds to the ISBT resonance of the structure. The imaginary component of the permittivity corresponds to material absorption. We can see in the inset of figure 3.5(a) that the imaginary permittivity is peaked at λ_{ISBT}=5 μm. Note that if the ISBT energy is tuned away from the range of wavelengths shown here, or is turned off completely, the resonance at λ_{ISBT} would not appear in the dispersion of the perpendicular permittivity ($\epsilon_{\perp}$).

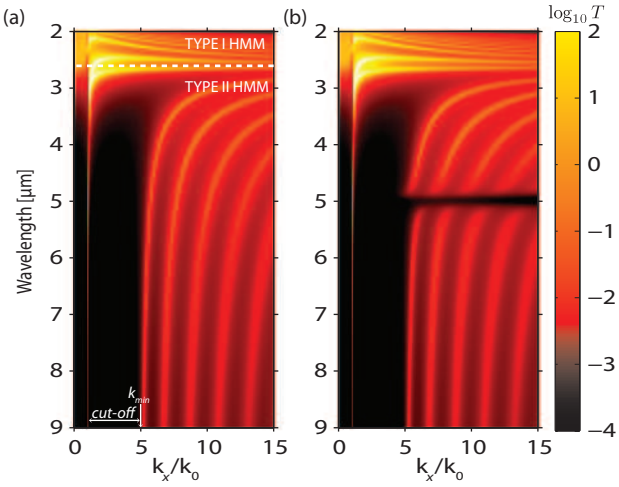

Figure 3.6: Transmission of an 800 nm thick homogenized MQW-InGaAs slab simulated with the transfer matrix method. (a) Type I and Type II high-k modes of the slab with intersubband transitions (ISBTs) of the slab tuned away from the mode energies. (b) Strong coupling between the ISBT and Type II modes of the slab at $\lambda_{ISBT} = 5\mu$m. A series of high-k-ISBT polaritons are formed. In both (a) and (b) the structure supports high-k modes up to infinitely large wavevectors. The cut-off region indicates the wavevectors for which no transmission is allowed through the slab until k_{min}, indicating the smallest wavevector for the 1st high-k mode in the defined wavelength range. k_0 is the free-space wavevector.

We use the dispersions shown in figure 3.5 and the transfer matrix method to evaluate the transmission for an 800 nm homogenized MQW-InGaAs slab (figure 3.6). Figure 3.6(a) shows the high-k modes for a semiconductor HMM with the ISBT resonance tuned away from the observed modes. Clear regions of the Type I and Type II modes are distinguishable and are in correspondence with the EMT parameters of figure 3.5. Note that due to the hyperbolic dispersion the k_x wavevector is unbounded in this EMT limit, and high-k modes up to wavevector magnitudes approaching infinity will be observed [6, 47].

A distinct cut-off region for the Type II modes is observed where there is no transmission through the metamaterial in k-space. The metamaterial is highly metallic and thus extremely reflective in the cut-off region. The appearance of high-k modes starts at the k_{min} point where conditions are satisfied to support the high-k modes

for the structure [6].

Figure 3.6(b) is identical to the semiconductor HMM shown in figure 3.6(a) however the ISBT resonance is tuned to $\lambda_{ISBT} = 5\mu$m so that it couples with the high-k modes of the metamaterial. It is immediately observed that anticrossing behaviour of each high-k mode occurs at the ISBT wavelength (λ_{ISBT}). Each high-k mode, upon coupling with the ISBT, gains a typical polariton like dispersion, reminiscent of strong coupling behaviour, creating one high-k-ISBT polariton. Strong coupling zones, whether it be particular wavevector regions or energies, can be assigned by tuning the ISBT energy or the dispersion profile of the modes [43]. Both of these parameters can be tuned by the quantum well thickness and period as well as the doping density of the semiconductors in the structure. Note, however, that the dispersion of the permittivity and the losses of the systems would need to be taken into consideration in order to ensure that conditions for strong coupling are met.

The magnitude of splitting observed can be quantified by extracting a specific high-k-ISBT polariton from the dispersions in figure 3.6(b) and matching it to the analytical expression of equation 3.9, using the VRS energy as a fitting parameter. The 4^{th} high-k ISBT polariton (for the region lying between 12-14 k_x/k_0) is extracted, as seen in figure 3.7, and plotted in conjunction with the analytical expression with a fitting parameter for the VRS energy at $\hbar\Omega = 38$meV.

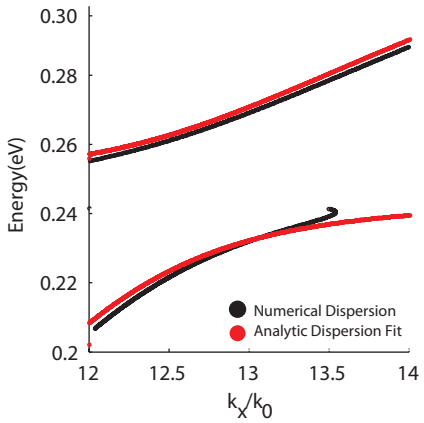

Figure 3.7: Analytic (equation 3.9) and numerical dispersions for the extracted 4^{th} high-k-ISBT polariton shown in figure 3.6(b). The magnitude of the splitting energy is determined by using the VRS energy as a fitting parameter in the analytical expression to match the numerical results. The fitting parameter $\hbar\Omega$=38 meV is used in the analytical expression.

There is a strong correlation between the numerical transfer matrix dispersion and the analytic dispersion of the 2 level model (equation 3.9) using the VRS fitting parameter (figure 3.7). This allows us to make a good approximation of the splitting energy for the 4^{th} high-k-ISBT polariton. However, we note that the lower branch

Table 3.1: Vacuum rabi splitting (VRS) energy between Type II HMM modes and the ISBT for the 800 nm thick homogenized MQW-InGaAs slab shown in figure 3.6. The magnitude of the VRS energy is decreasing with increasing Type II mode number and wavevector.

High-k ISBT	k_x/k_0 Bounds	VRS Energy ($\hbar\Omega$) [meV]
1	5-6.6	45
2	6.9-8.7	41
3	9-11.2	39
4	12-15	38

starts back-bending at higher values of the in-plane wavevector (k_x) in the simulated curve. This can be attributed to the loss and imperfections of the system, showing behaviour related to lossy polaritons. The analytical expression of equation 3.9 does not take the back-bending behaviour due to such losses into account, however the magnitude of the VRS energy determined is still a valid approximation as seen with the strong correlation between the simulated and analytic results.

The approximated VRS energies for all the high-k-ISBT polaritons (Table 3.1) show that the maximum splitting occurs with the first polariton, with a VRS energy ≈ 9 times greater than the ISBT linewidth for the homogenized structure. This is sufficient to satisfy the strong coupling requirement between the high-k states and the ISBT.

We also note that the magnitude of the VRS Energy decreases with increasing values of the in-plane wavevector (k_x). This is explained by observing that the maximum amplitude of the electric fields in the growth direction (E_z) also decreases with k_x and the Type II mode number. This is outlined in figure 3.9 using the in-plane magnetic fields ($|B_y|$). We use ($|B_y|$) instead of the discontinous perpendicular electric fields ($|E_z|$) for the sake of clarity. The ISBT, for the coordinate axis assigned to the structure in this paper, requires z-polarized E-fields for the transition to be allowed as a result of orthogonality conditions, as outlined in section 3.2.2. The strength of the ISBT is dependent on the magnitude of the electric fields normal to the interface and, as a result, the decreasing E_z field magnitude leads to a decreased ISBT absorption. The decreased strength of the transition leads to reduced coupling with the high-k mode and the overall VRS energy is decreased.

3.5 Type II Semiconductor HMMs: Practical Realization

The EMT calculations of section 3.4 are now validated with a practical multilayer approach for the semiconductor HMM. Here, the transmission of the incident radiation through each individual layer of the structure is determined with the transfer matrix method. Determination of optical properties in this fashion is more representative of a structure conceived in fabrication.

Analysis of the transmission spectra of the semiconductor HMM, obtained through the numerical transfer matrix method, shows strong coupling behaviour between the intersubband transitions in a practical multilayer structure (figure 3.8) with results comparable to those seen with EMT (figure 3.6). The multilayer structure analyzed here here consists of 5 layers of a 80 nm MQW slab alternated with 5 layers of 80 nm n^+-InGaAs semiconductor for a total structure thickness of 800 nm. Note that the total thickness of the structure is the same thickness as the analysis done with the EMT slab in section 3.4.

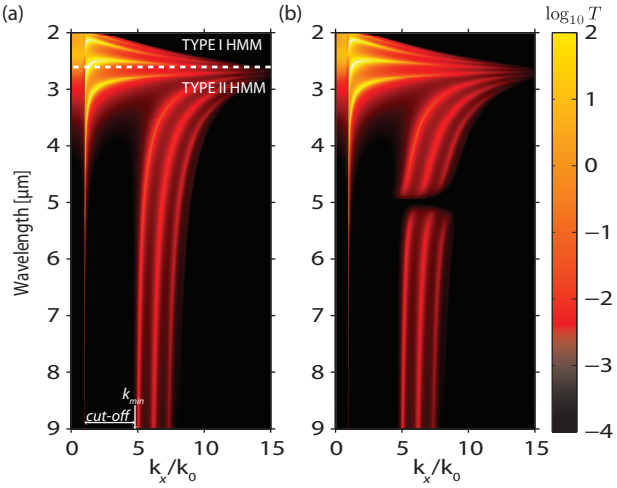

Figure 3.8: Transmission of 10 alternating MQW and InGaAs 80 nm layers using the transfer matrix method. (a) Type I and Type II high-k modes of the multilayer structure with intersubband transitions (ISBTs) tuned away from the mode energies. (b) Strong coupling between the ISBT and Type II modes of the multilayer structure at $\lambda_{ISBT} = 5\mu$m. A series of high-k-ISBT polaritons are formed. In both (a) and (b) the multilayer structure shows strong agreement with the effective medium results of figure 3.6. Note that the multilayer structure, in comparison to the homogenized slab, experiences an upper cutoff of the wavevector as it approaches the size of the unit cell. The cut-off region for wavevectors smaller than k_{min} shows a match to EMT (figure 3.6). k_0 is the free-space wavevector.

Figure 3.8 shows very good agreement with the EMT dispersions shown in figure

Table 3.2: Vacuum rabi splitting (VRS) energy between Type II HMM modes and the ISBT for the MQW-InGaAs multilayer structure shown in figure 3.8. The magnitude of the VRS energy is decreasing with increasing Type II mode number and wavevector, similar to the results seen in Table 3.1 for the homogenized MQW-InGaAs slab

High-k ISBT	k_x/k_0 Bounds	VRS Energy ($\hbar\Omega$) [meV]
1	4.5-6.2	52
2	6.6-7.6	48
3	7.8-8.8	47

3.6, including the mode profile of the high-k modes as well as the strong coupling behaviour with the ISBT. The multilayer structure, however, has a distinct upper cut-off for the high-k modes that was not seen in the EMT structure. At larger wavevector values the waves begin propagating with effective wavelengths comparable to the size of the unit cell and no longer see the structure as an effective medium. The wavevectors lie at the edge of the brillioun zone of the periodic lattice and begin to bragg scatter, leading to an upper limit in which potential high-k modes can propagate in the multilayer structure. The transfer matrix method takes the size of the unit cell into account, and thus in the multilayer semiconductor HMM (figure 3.8), a sharp upper cut-off is observed at the point where the wavevector becomes comparable to the unit cell size [6].

The magnitude of the strong coupling in the multilayer structure was extracted by comparing the analytical expression of equation 3.9 with the numerical results in the same manner as was done with the EMT slab (section 3.4). It is noted that in the multilayer structure only 3 high-k-ISBT polaritons are present in comparison to the 4 seen with the EMT slab of the same thickness due to the upper cut-off wavevector of the multilayer structure. As expected, the maximum VRS energy ($\hbar\Omega$= 52 meV) occurs for the first high-k-ISBT polariton for the system, a value $\approx$ 10.5 times greater than the ISBT linewidth.

Again, similar to the EMT slab, decreasing values of the VRS energy are seen for larger values of the in-plane wavevector (k_x) and increasing high-k-ISBT polariton mode number (figure 3.9). The magnitude of the in-plane magnetic fields (B_y) also decreases with increasing k_x for the multilayer structure, matching the observations seen in EMT.

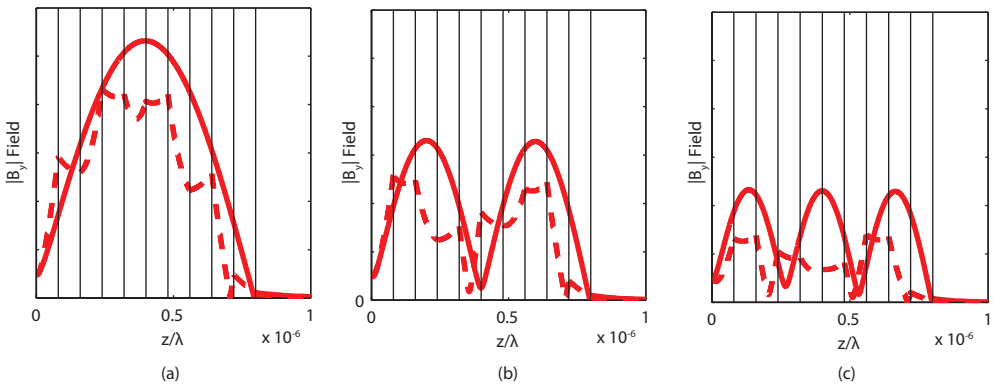

Figure 3.9: Relative magnitudes of the in-plane magnetic field ($|B_y|$) at a wavelength of 5 μm for the first 3 high-k modes of the MQW-InGaAs multilayer(dashed) and homogenized(solid) structure. The continuous $|B_y|$ fields instead of the discontinuous electric fields in the growth direction ($|E_z|$) are shown for clarity. The decreasing magnitude of the $|B_y|$ (and $|E_z|$) field correlates with the decreasing VRS energy of the high-k-ISBT polaritons at higher values of the in-plane wavevector(k_x) as the ISBT absorption strength is dependent on the field magnitude.

3.6 Summary

In this chapter, we proposed a design for an active multilayer semiconductor structure able to achieve hyperbolic dispersion in the mid-IR. The structure consists of an alternating active dielectric component with embedded quantum wells and metallic component composed of a degenerately doped semiconductor.

We simulated strong coupling interactions between the high-k modes of the HMM and the intersubband transitions of the quantum wells with vacuum rabi splitting energies up to 52 meV. The system showed strong coupling behaviour using the effective medium approach as well with a practical structure. The numerical strong coupling dispersion showed strong agreement when compared to a semiclassical analytic expression describing the anti-crossing behaviour of strongly coupled systems.

This is the first example of strong coupling behaviour in hyperbolic metamaterials. In this chapter, we have presented the initial steps toward realizing quantum optic effects in hyperbolic media.

Chapter 4

Superradiance in Semiconductor HMM Systems

4.1 Introduction to Superradiance

Superradiance describes the process of a collection of emitters behaving as an ensemble such that their collective decay rate is coherently increased [10]. Superradiant behaviour between a collection of emitters was originally discovered by Dicke in 1954 and has promising uses for detecting specific atomic states as well as controlling coherent processes between multiple atoms. Unlike stimulated emission processes, superradiance is a manifestation of a coherent spontaneous emission process that arises due to the interaction of the radiation fields of very closely spaced emitters. The emitters must be placed close enough (much closer than the radiation wavelength) such that near-field coupling between the emitters is possible in order to induce the coherent effects [11].

If a collection of N dipoles are in a superradiant state and emit coherently, the intensity of the emission expectedly scales as N^2 due to the constructive interference of the radiating fields. Additionally, if the N dipoles are initially in their excited state there is an increase of the radiative decay rate (Γ) by a factor N. Specifically, dipoles in a superradiant state have a collective radiative decay rate of $N\Gamma$ [10].

Section 2.4.3 discussed how controlling the photonic density of states (PDOS) can lead to large radiative decay rate enhancements. Superradiant behaviour can also be mediated by controlling the PDOS. Recent work has shown how superradiant behaviour between largely spaced emitters can be mediated by surface plasmon polaritons [48, 49, 50, 51] as well as epsilon near zero (ENZ) materials [52] to induce the near field coupling. In this chapter we look to see if it is possible to mediate superradiant behaviour in similar fashion with the high-k modes of a semiconductor HMM.

4.2 Decay Rate of Enhancement of a Quantum Emitter

The large decay rate enhancement (section 2.4.3) of a single emitter placed near a hyperbolic metamaterial has been widely studied by a number of groups [9, 23, 28, 29, 31]. Here, we first look to see if a single dipole placed above a semiconductor hyperbolic metamaterial shows the same broadband decay rate enhancement that has been seen in previous studies with other HMMs [8, 9, 23]. First, we need to determine the dispersion of the semiconductor HMM so we have a better understanding as to the details of the high-k modes in the system. We will see that the emitter couples into these high-k modes.

The transmission through a 5 μm semiconductor HMM slab showing the Type I modes of the semiconductor HMM is shown in figure 4.1.

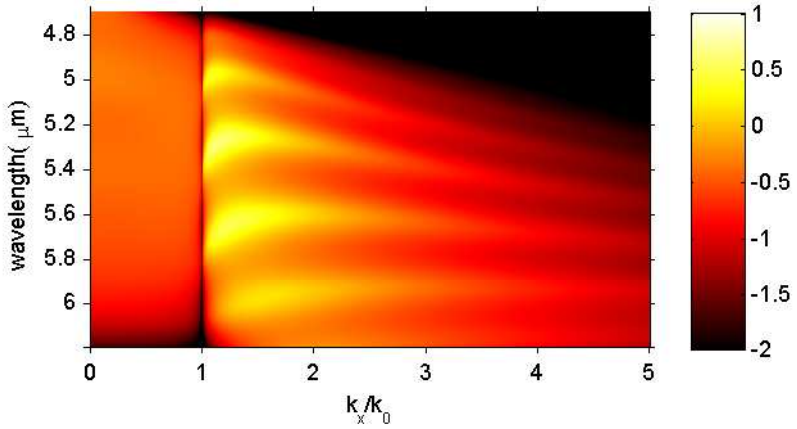

Figure 4.1: Transmission through a 5 μm semiconductor HMM for a region of the spectrum in the Type I region using the transfer matrix method. The bands are the Type I high-k modes of the structure and the bright regions at $\frac{k_x}{k_0} \approx 1.3$ near zero group velocity are the Van Hove singularities in the dispersion. k_x is the in-plane wavevector and k_0 is the freespace wavevector.

The series of bands seen in the transmission spectra in figure 4.1 are the Type I high-k modes of the system. Note the Type I region of the dispersion corresponds to permittivities with a negative perpendicular component ($\epsilon_\perp < 0$) and positive parallel component ($\epsilon_\parallel > 0$) forming the two sheeted hyperbolic dispersion (section 2.2.

The bright regions with a high PDOS on each of the bands at $\frac{k_x}{k_0} \approx 1.3$ are analogous to the electronic Van Hove Singularities in the dispersion [53]. Specifically, in the low loss limit, the photonic density of states is inversely proportional to the group velocity. It is seen that as these high-k modes transition from positive to negative group velocities near $\frac{k_x}{k_0} \approx 1.3$, they pass through the point of zero group velocity. As a result, there is a relatively larger enhancement of the PDOS in this

region leading to enhanced emitter coupling into the semiconductor HMM. This shows up as the brighter regions in the transmission spectrum in figure 4.1.

We calculate the decay rate enhancement (Γ_{11}/Γ_0) for an emitter close to the top interface of the semiconductor HMM using the Green's function formalism as outlined in section 2.4.3. Here Γ_{11} is the decay rate computed in the near-field of the HMM and Γ_0 is the decay rate in free space. Throughout this thesis we work in the point dipole approximation and emphasize that the semiclassically computed decay rate is exactly equivalent to the quantum electrodynamic result in the weak-coupling limit. Figure 4.2 shows the enhancement for a single quantum emitter placed at different distances from the top semiconductor HMM interface.

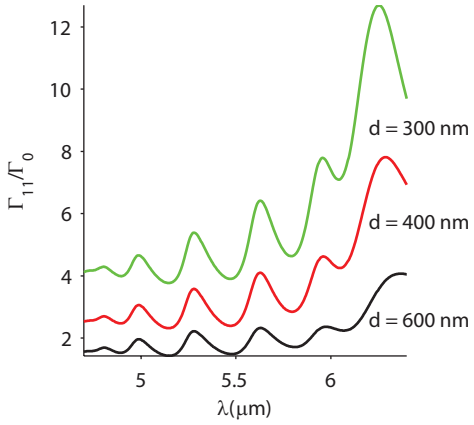

Figure 4.2: Decay rate enhancement of a single emitter placed at different distances (d) above a 5 μm semiconductor HMM with dispersion shown in figure 4.1. $\frac{\Gamma_{11}}{\Gamma_0}$ is the decay rate enhancement normalized to free space of 1 emitter above the slab coupling with the high-k modes of the HMM. Broadband enhancement is seen for all emitter distances above the slab with peaks occurring at the Van Hove singularities in the dispersion.

This decay rate enhancement occurs due to the coupling with the high-k modes of the semiconductor HMM. Furthermore, we can get coupling with inhomogeneously broadened emitters at room temperature since the hyperbolic modes occur in a broad bandwidth. In figure 4.2 we see that the number of high-k states present, as shown in figure 4.1, causes a broadband decay rate enhancement. Specifically, the enhancement is greater than 1 for all the emitter distances for the region of the spectrum shown. There are peaks in the enhancements at wavelengths corresponding to the Van Hove singularities in the metamaterial [53]. The Van Hove singularities occur at the wavelengths where the hyperbolic mode has slow group velocity. This is evident from the flat dispersion in this region as can be seen in figure 4.1. The largest peak at $\lambda \approx 6.2$ μm is due to epsilon-near-zero behaviour at the optical

topological transition resonance [31]. We see an overall increase of the decay rate enhancement as the emitter is moved closer to the semiconductor HMM due to the increased near field coupling to the high-k modes of the structure.

4.3 The Non-local Density of States

In section 4.2 it was observed how a single emitter can weak couple to a semiconductor HMM leading to a Purcell factor enhancement. The next step is to see the observed effect of placing a second emitter into the system that can potentially couple with the original emitter. Figure 4.3 shows a schematic and field plot of the system where the effect of the decay rate on the top emitter will be studied as a function of the distance(d) of both the top and the bottom emitter from the slab. In this thesis we will be looking specifically at symmetric systems.

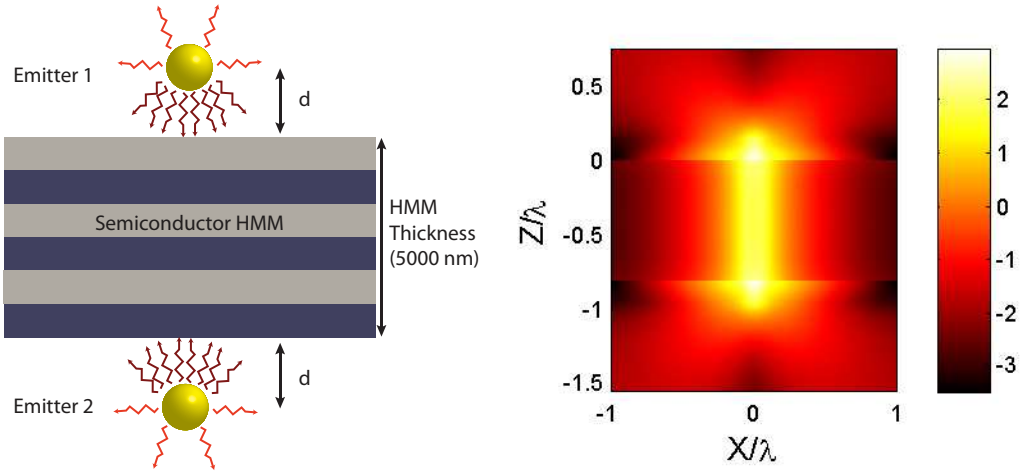

Figure 4.3: Schematic showing an emitter placed at a distance d above and below a 5 μm thick semiconductor HMM (left). The coupling between the two emitters will be mediated by the HMM structure. Log of the electric field intensity of two dipoles coupled with a 5 μm thick semiconductor HMM as a function of the position in the x and y directions normalized by the emitter wavelength (right). Both dipoles are coupling into a Type I mode of the semiconductor HMM structure.

We now introduce the central concept which governs superradiance, the nonlocal photonic density of states. This defines the resultant photonic density of states due to the influence of the second emitter at a position r_i on an emitter at positon r_j. We saw in equation 2.13 that we can define the decay rate of an emitter in terms of the local density of states. We can define the decay rate of an emitter due to the nonlocal density of states as follows [48]:

$$\Gamma_{ij} = \frac{2\omega_0}{\pi c^2 \epsilon_0 \hbar} \Im[\mu_i^* \cdot G(r_i, r_j) \cdot \mu_j] \tag{4.1}$$

Equation 4.1 describes the influence on the decay rate of an emitter (in the point dipole approximation) placed at position i (above the slab) with dipole moment μ_i due to an emitter at position j (below the slab) with dipole moment μ_j. $\Im$ denotes that we are taking the imaginary component of the Green's function. If we define the emitter above the slab as position 1 and the emitter below the slab as position 2, Γ_{12} is then the contribution to the decay rate of the emitter at position 1 due to the change in the nonlocal density of states caused by the emitter at position 2 [48]. We note that the influence of the environment on the non-local density of states is present in the Green's function.

The fact that we are dealing with linear set of equations allows us to define the total decay rate of the emitter at position 1 as the sum of the contributions from the local and non-local density of states:

$$\Gamma_{SR} = \Gamma_{11} + \Gamma_{12} \tag{4.2}$$

Here the subscript "SR" refers to potential 'superradiant' behaviour of the decay rate of the emitter at position 1 due the local and non-local density of states. In section 4.4 we will see the influence a hyperbolic metamaterial has on the Γ_{SR} term within a system.

4.4 Superradiance With Hyperbolic Metamaterials

In section 4.1 we saw that near field coupling between the emitters is necessary in order to induce the coherent effects required for superradiant behaviour. Hyperbolic metamaterials provide an avenue for potentially mediating superradiant behaviour between two emitters across distances larger than the radiation wavelength. The high-k states of the HMM can be used to create this near field coupling between the two emitters across the length of the HMM slab.

In section 4.2, we saw that a single emitter placed in the near field of a semiconductor HMM effectively couples to the high-k states. This is manifested in the enhancement of the emitter decay rate. We can similarly determine the coupling between an emitter at position 1 on top of the slab and an emitter at position 2 below the slab by normalizing it to the enhancement seen by a single emitter.

Figure 4.4(a) shows the enhancement to the decay rate of an emitter located at position 1 due to both the local and nonlocal density of states (Γ_{SR}) for a 5 μm thick semiconductor HMM with a dispersion shown in figure 4.1.

In figure 4.4(a) we see that each peak of Γ_{SR} is alternatively enhanced and suppressed in comparison to Γ_{11} (figure 4.2). This can be better understood if we look at figure 4.4(b). Figure 4.4(b) shows the field intensity at the position of the top emitter ($d = 300$ nm) for both the 1 emitter and 2 emitter case. We can see that

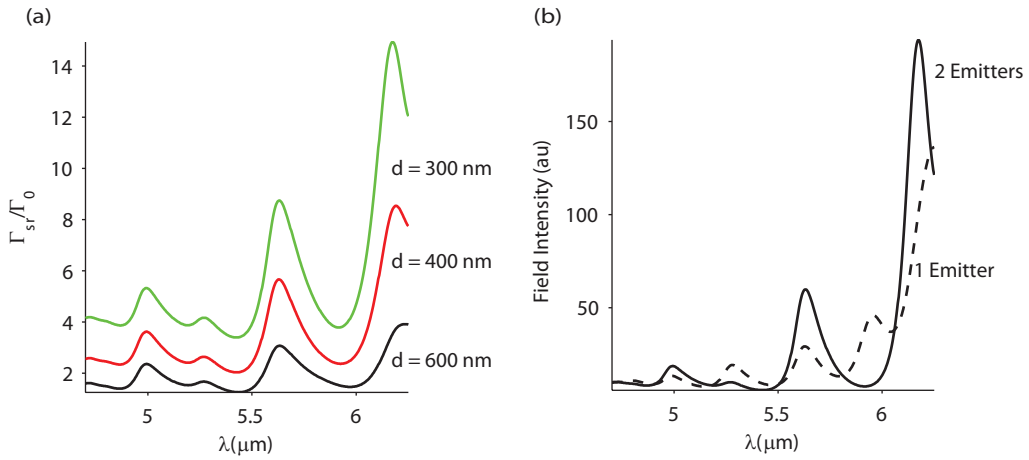

Figure 4.4: (a) Radiative decay rate enhancement of an emitter located at different distances (d) above a 5 μm thick semiconductor HMM with dispersion given in figure 4.1. Decay rate enhancement relative to free space ($\frac{\Gamma_{SR}}{\Gamma_0}$) takes both the local density of states and the nonlocal density of states from an emitter located symmetrically opposite below the slab into account.(b) Field intensity for $d = 300$ nm at the position of the emitter above the slab for both the single emitter case and the 2 emitter case. Comparison to the $d = 300$ nm case in (a) shows regions of highest decay rate enhancement correspond with regions of highest field intensity due to constructive interference between the two emitters.

magnitude of the field intensities for the single emitter case are also alternatively enhanced and suppressed in comparison to the 2 emitter case. Specifically, we are seeing that the even (symmetric) modes constructively interfere and that the odd (anti-symmetric) modes destructively interfere for the 2 emitters interacting across the HMM slab. As a result, we see enhanced coherent decay rates for the 2 emitters case where there is constructive interference and suppressed decay rates for where there is destructive interface. Phase, therefore, is playing a key role in mediating the coherent spontaneous emission between the 2 emitters in the system.

Figure 4.5(a) shows a clearer picture for the regions of enhanced decay rates and suppressed decay rates by normalizing Γ_{SR} with Γ_{11} for different emitter distances from the HMM slab. Regions where $\frac{\Gamma_{SR}}{\Gamma_{11}} > 1$ shows an enhanced coherent decay rate and regions with $\frac{\Gamma_{SR}}{\Gamma_{11}} < 1$ show a suppressed coherent decay rate as a result of the constructive and destructive interference respectively.

Figure 4.5(b) shows the same enhancement factor as a function of the distance (d) of both the bottom and top emitter from the slab. We see a clear dependence of the enhancement factor ($\frac{\Gamma_{SR}}{\Gamma_0}$) on the emitter distance and note that there is an ideal distance where the fields from both emitters constructively interfere resulting in the largest enhancement factor. We see further proof of this upon comparing figure 4.5(a) and figure 4.5(b) where largest degree of suppression and enhancement

of the decay rate occurs at $d = 400$ nm.

Overall, with two emitters in a superradiant state we should see a coherent decay rate enhancement factor ($\frac{\Gamma_{SR}}{\Gamma_{11}}$) of 2. The largest value we see for this particular semiconductor HMM system is ≈ 1.35 however the distance between the emitters is on the order of a wavelength. Normally, superradiant behaviour in vacuum requires near field coupling with emitter distances approximately one-tenth of the wavelength. It is likely that the semiconductor HMM is mediating near-field coupling between the two emitters as there is comparatively no enhancement seen in vacuum at such large distances. However, due to the relatively large thickness of the slab and the losses in the system the enhancement factor is limited. In chapter 5 we discuss possible avenues for improving this result in the future.

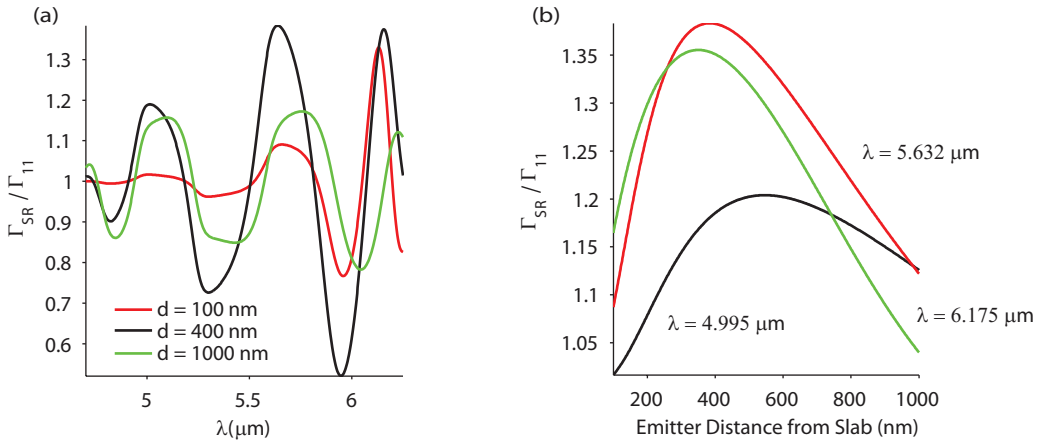

Figure 4.5: (a) Total coherent decay rate enhancement from local and non-local density of states (Γ_{SR}) normalized by decay rate enhancement for a single emitter (Γ_{11}). Regions of enhanced decay rates ($\frac{\Gamma_{SR}}{\Gamma_{11}} > 1$) are due to the constructive interference between the 2 emitters. Conversely, regions of suppressed decay rates ($\frac{\Gamma_{SR}}{\Gamma_{11}} < 1$) relative to 1 emitter above the HMM slab are a result of destructive interference between the two emitters. (b) Total coherent decay rate enhancement for 2 emitters normalized by decay rate for a single emitter as a function of emitter distance (d) from the top and bottom of the slab for different wavelengths (λ). The maximum decay rate enhancement is seen at emitter distances resulting in the largest constructive interference between the two emitters, showing the phase dependence on the enhancement factor.

4.5 Summary

Superradiance describes the process of a collection of emitters behaving as an ensemble such that their collective decay rate is coherently increased [10]. In vacuum, superradiant phenomena is only possible between very closely spaced emitters as a

result of their near field coupling.

In this chapter, we showed that superradiant behaviour can be mediated across large distances on the order of the radiation wavelength. This was made possible by using the high-k states of semiconductor HMM to couple the near-fields of emitters at the top and bottom of the structure.

Decay rate enhancements of up to ≈ 1.35 times greater than vacuum were achieved with the semiconductor HMM. It was determined that the phase difference between the two emitters across the slab can either suppress or enhance the decay rate as a result of destructive and constructive interference respectively. Also, it was found that the overall collective decay rate enhancement is limited due to losses in the semiconductor HMM structure. We believe the overall enhancement factor can be further improved in future studies. This is the first example of superradiant behaviour in hyperbolic metamaterials and opens the door for observing new coherent phenomena in such media.

Chapter 5

Future Work

In this thesis, we looked at the necessary first steps towards understanding quantum phenomena in hyperbolic metamaterials. Up until now significant work has explored the weak coupling limit by enhancing the decay rate of an emitter placed close to an HMM. Here, we showed that it is possible to design semiconductor hyperbolic metamaterials where the embedded quantum wells of the structure can indeed strongly couple to unique metamaterial modes. The quantum wells proved to be an ideal system to allow for subwavelength integration into the metamaterial. Additionally, the losses in the HMM were mitigated by the large oscillator strength of the many embedded emitters provided by the multiple quantum wells. These factors allowed to create the strong interaction necessary to witness strong coupling behaviour in the system. The fact that we used many emitters embedded within the structure suggests that we have defined strong coupling in this system in the semi-classical limit. Observing strong coupling in this semi-classical limit is the first necessary stepping stone to realizing true quantum phenomena in HMMs. The future work will consist of moving from the semiclassical approach to quantum optical treatment in two directions.

First, in the strong coupling regime, it is necessary to move from the many embedded emitters provided by the embedded quantum wells to the single emitter regime. This will allow us to define a purely quantum mechanical system. It will be necessary to see whether strong coupling is still supported in such systems due to the decrease in the emitter oscillator strength and the lossy nature of the HMM. Once this is established, true quantum coherent effects in HMMs can be explored.

The second approach involves expanding on the preliminary work discussed in chapter 4 regarding superradiant behaviour between a pair of emitters mediated by an HMM slab. The preliminary work does show an enhancement to the collective radiative decay rate in comparison to vacuum, however, further work can be done to improve the coupling. This includes looking at alternate materials, material geometry, type of modes, and reducing the loss to improve the results. A full

quantum treatment for superradiant behaviour can also be done, in which case, further work will need to be incorporated into the current models used. We also plan to explore the initial experimental conditions needed to prepare the quantum emitters in a superradiant excited state.

Bibliography

[1] Vladimir M Shalaev. Optical negative-index metamaterials. *Nature Photonics*, 1(1):41–48, January 2007.

[2] L Menon, W T Lu, A L Friedman, S P Bennett, D Heiman, and S Sridhar. Negative index metamaterials based on metal-dielectric nanocomposites for imaging applications. *Applied Physics Letters*, 93(12):123117, September 2008.

[3] S Foteinopoulou, E N Economou, and C M Soukoulis. Refraction in Media with a Negative Refractive Index. *Physical Review Letters*, 90(10):107402, March 2003.

[4] Zubin Jacob, Leonid V Alekseyev, and Evgenii Narimanov. Optical Hyperlens: Far-field imaging beyond the diffraction limit. *Optics Express*, 14(18):8247–8256, September 2006.

[5] Zhaowei Liu, Stéphane Durant, Hyesog Lee, Yuri Pikus, Nicolas Fang, Yi Xiong, Cheng Sun, and Xiang Zhang. Far-Field Optical Superlens. *Nano Letters*, 7(2):403–408, February 2007.

[6] C L Cortes, W Newman, S Molesky, and Z Jacob. Quantum nanophotonics using hyperbolic metamaterials. *Journal of Optics*, 14(6):63001, June 2012.

[7] Alexander A Govyadinov and Viktor A Podolskiy. Metamaterial photonic funnels for subdiffraction light compression and propagation. *Physical Review B*, 73(15):155108, April 2006.

[8] Zubin Jacob, Igor I Smolyaninov, and Evgenii E Narimanov. Broadband Purcell effect: Radiative decay engineering with metamaterials. *Applied Physics Letters*, 100(18):181104–181105, May 2012.

[9] M A Noginov, H Li, Yu. A Barnakov, D Dryden, G Nataraj, G Zhu, C E Bonner, M Mayy, Z Jacob, and E E Narimanov. Controlling spontaneous emission with metamaterials. *Optics Letters*, 35(11):1863–1865, June 2010.

[10] R H Dicke. Coherence in Spontaneous Radiation Processes. *Physical Review*, 93(1):99–110, January 1954.

[11] Marlan O Scully and Anatoly A Svidzinsky. The Super of Superradiance. *Science*, 325(5947):1510–1511, September 2009.

[12] L D Landau, E M Lifshits, and L P Pitaevski. *Electrodynamics of continuous media*. Butterworth-Heinemann, Oxford [England], 1995.

[13] Anthony J Hoffman, Leonid Alekseyev, Scott S Howard, Kale J Franz, Dan Wasserman, Viktor A Podolskiy, Evgenii E Narimanov, Deborah L Sivco, and Claire Gmachl. Negative refraction in semiconductor metamaterials. *Nature Materials*, 6(12):946–950, December 2007.

[14] M A Noginov, Yu A Barnakov, G Zhu, T Tumkur, H Li, and E E Narimanov. Bulk photonic metamaterial with hyperbolic dispersion. *Applied Physics Letters*, 94(15):151105, April 2009.

[15] Justin Elser, Robyn Wangberg, Viktor A Podolskiy, and Evgenii E Narimanov. Nanowire metamaterials with extreme optical anisotropy. *Applied Physics Letters*, 89(26):261102, December 2006.

[16] Jie Yao, Zhaowei Liu, Yongmin Liu, Yuan Wang, Cheng Sun, Guy Bartal, Angelica M Stacy, and Xiang Zhang. Optical Negative Refraction in Bulk Metamaterials of Nanowires. *Science*, 321(5891):930, August 2008.

[17] R J Pollard, A Murphy, W R Hendren, P R Evans, R Atkinson, G A Wurtz, A V Zayats, and Viktor A Podolskiy. Optical Nonlocalities and Additional Waves in Epsilon-Near-Zero Metamaterials. *Physical Review Letters*, 102(12):127405, March 2009.

[18] B D F Casse, W T Lu, Y J Huang, E Gultepe, L Menon, and S Sridhar. Super-resolution imaging using a three-dimensional metamaterials nanolens. *Applied Physics Letters*, 96(2):23114, January 2010.

[19] Alexandra Boltasseva and Harry A Atwater. Low-Loss Plasmonic Metamaterials. *Science*, 331(6015):290–291, January 2011.

[20] P.r. West, S Ishii, G.v. Naik, N.k. Emani, V.m. Shalaev, and A Boltasseva. Searching for better plasmonic materials. *Laser & Photonics Reviews*, 4(6):795–808, 2010.

[21] Jonathan Plumridge and Chris Phillips. Ultralong-range plasmonic waveguides using quasi-two-dimensional metallic layers. *Physical Review B*, 76(7), August 2007.

[22] Lukas Novotny and Bert Hecht. *Principles of Nano-Optics*. Cambridge University Press, Cambridge, 2 edition, 2012.

[23] Z Jacob, J.-Y. Kim, G V Naik, A Boltasseva, E E Narimanov, and V M Shalaev. Engineering photonic density of states using metamaterials. *Applied Physics B*, 100(1):215–218, July 2010.

[24] P Michler, A Kiraz, C Becher, W V Schoenfeld, P M Petroff, Lidong Zhang, E Hu, and A Imamoglu. A Quantum Dot Single-Photon Turnstile Device. *Science*, 290(5500):2282–2285, December 2000.

[25] Matthew Pelton, Charles Santori, Jelena Vucković, Bingyang Zhang, Glenn S Solomon, Jocelyn Plant, and Yoshihisa Yamamoto. Efficient Source of Single Photons: A Single Quantum Dot in a Micropost Microcavity. *Physical Review Letters*, 89(23):233602, November 2002.

[26] Peter Lodahl, A van Driel, Ivan S Nikolaev, Arie Irman, Karin Overgaag, Daniël Vanmaekelbergh, and Willem L Vos. Controlling the dynamics of spontaneous emission from quantum dots by photonic crystals. *Nature*, 430(7000):654–657, August 2004.

[27] S Hughes. Enhanced single-photon emission from quantum dots in photonic crystalwaveguides and nanocavities. *Optics Letters*, 29(22):2659–2661, November 2004.

[28] Alexander N Poddubny, Pavel A Belov, and Yuri S Kivshar. Spontaneous radiation of a finite-size dipole emitter in hyperbolic media. *Physical Review A*, 84(2):23807, August 2011.

[29] Omar Kidwai, Sergei V Zhukovsky, and J E Sipe. Dipole radiation near hyperbolic metamaterials: applicability of effective-medium approximation. *Optics letters*, 36(13):2530–2, July 2011.

[30] Zubin Jacob and Vladimir M Shalaev. Plasmonics Goes Quantum. *Science*, 334(6055):463–464, October 2011.

[31] Harish N S Krishnamoorthy, Zubin Jacob, Evgenii Narimanov, Ilona Kretzschmar, and Vinod M Menon. Topological Transitions in Metamaterials. *Science*, 336(6078):205–209, April 2012.

[32] Brahim Lounis and Michel Orrit. Single-photon sources. *Reports on Progress in Physics*, 68(5):1129, May 2005.

[33] G W Ford and W H Weber. Electromagnetic interactions of molecules with metal surfaces. *Physics Reports*, 113(4):195–287, November 1984.

[34] G Khitrova, H M Gibbs, M Kira, S W Koch, and A Scherer. Vacuum Rabi splitting in semiconductors. *Nature Physics*, 2(2):81–90, 2006.

[35] Ralf Ameling, Daniel Dregely, and Harald Giessen. Strong coupling of localized and surface plasmons to microcavity modes. *Optics Letters*, 36(12):2218–2220, June 2011.

[36] A V Rogacheva, V A Fedotov, A S Schwanecke, and N I Zheludev. Giant Gyrotropy due to Electromagnetic-Field Coupling in a Bilayered Chiral Structure. *Physical Review Letters*, 97(17):177401, October 2006.

[37] D J Shelton, I Brener, J C Ginn, M B Sinclair, D W Peters, K R Coffey, and G D Boreman. Strong Coupling between Nanoscale Metamaterials and Phonons. *Nano Letters*, 11(5):2104–2108, May 2011.

[38] D Steinbach, G Kocherscheidt, M U Wehner, H Kalt, M Wegener, K Ohkawa, D Hommel, and V M Axt. Electron-phonon quantum kinetics in the strong-coupling regime. *Physical Review B*, 60(17):12079–12090, November 1999.

[39] D E Chang, P R Hemmer, and M D Lukin. Quantum Optics with Surface Plasmons. pages 1–11, 2008.

[40] V Agranovich, M Litinskaia, and D Lidzey. Cavity polaritons in microcavities containing disordered organic semiconductors. *Physical Review B*, 67(8), February 2003.

[41] M Zauny and C Nalewajko. Coupling of infrared radiation to intersubband transitions in multiple quantum wells: The effective-medium approach. *Physical Review B*, 59(20):13043–13053, May 1999.

[42] Lukas Novotny. Strong coupling, energy splitting, and level crossings: A classical perspective. *American Journal of Physics*, 78(11):1199, 2010.

[43] Dimitri Dini, Rüdeger Köhler, Alessandro Tredicucci, Giorgio Biasiol, and Lucia Sorba. Microcavity Polariton Splitting of Intersubband Transitions. *Physical Review Letters*, 90(11):1–4, March 2003.

[44] Jonathan Plumridge, Edmund Clarke, Ray Murray, and Chris Phillips. Ultra-Strong Coupling Effects with Quantum Metamaterials. *arXiv:cond-mat/0701775*, January 2007.

[45] M S Skolnick, T A Fisher, and D M Whittaker. Strong coupling phenomena in quantum microcavity structures. *Semiconductor Science and Technology*, 13(7):645–669, July 1998.

[46] R Houdré, R P Stanley, U Oesterle, M Ilegems, and C Weisbuch. Room-temperature cavity polaritons in a semiconductor microcavity. *Physical Review B*, 49(23):16761–16764, June 1994.

[47] Yu Guo, Ward Newman, Cristian L. Cortes, and Zubin Jacob. Applications of Hyperbolic Metamaterial Substrates. *Advances in OptoElectronics*, 2012(1):1–9, 2012.

[48] Diego Martín-Cano, Luis Martín-Moreno, Francisco J García-Vidal, and Esteban Moreno. Resonance Energy Transfer and Superradiance Mediated by Plasmonic Nanowaveguides. *Nano Letters*, 10(8):3129–3134, August 2010.

[49] P A Huidobro, A Y Nikitin, C González-Ballestero, L Martín-Moreno, and F J García-Vidal. Superradiance mediated by graphene surface plasmons. *Physical Review B*, 85(15):155438, April 2012.

[50] J J Choquette, Karl-Peter Marzlin, and B C Sanders. Superradiance, subradiance, and suppressed superradiance of dipoles near a metal interface. *arXiv:1007.5259*, July 2010.

[51] S Aberra Guebrou, C Symonds, E Homeyer, J C Plenet, Yu. N Gartstein, V M Agranovich, and J Bellessa. Coherent Emission from a Disordered Organic Semiconductor Induced by Strong Coupling with Surface Plasmons. *Physical Review Letters*, 108(6):66401, February 2012.

[52] Romain Fleury and Andrea Alu. Enhanced Super-Radiance in Epsilon-Near-Zero Plasmonic Channels. *arXiv:1303.3510*, March 2013.

[53] Cristian L. Cortes and Zubin Jacob. Photonic analog of a van Hove singularity in metamaterials. *Physical Review B*, 88(4):045407, July 2013.

Appendix A

Green's Tensor Formalism

A.1 Introduction

Generally, the mathematical Green's function technique can be understood as a spatial extension of the impulse response formalism employed in introductory signals and systems. In such descriptions, a complete temporal relation between cause and effects is built up by considering a systems response to an unitary impulse input.

Building on this notion, the Green's function technique is a prescription for fully describing the spatial and temporal correlation of inputs and outputs based on point sources.

Mathematical Description. One dimensional time independent example: Φ a one dimensional function, $\hat{D}$ a one dimensional operator, $G(x, x')$ the greens function of the solution, δ the delta Dirac function and f(x) a source term.[1]

$$\hat{D}\langle\Phi\rangle = f(x) \tag{A.1}$$

$$\hat{D}\left\langle G(x,x')\right\rangle = \delta(x-x') \tag{A.2}$$

$$f(x')\hat{D}\left\langle G(x,x')\right\rangle = f(x')\delta(x-x') \tag{A.3}$$

$$\int f(x')\hat{D}\left\langle G(x,x')\right\rangle \mathrm{d}x = f(x) \tag{A.4}$$

$$\hat{D}\left\langle \int f(x')G(x,x')\mathrm{d}x \right\rangle = f(x) \tag{A.5}$$

Leading to the conclusion that Φ may be represented as

$$\boxed{\Phi = \int f(x')G(x,x')\mathrm{d}x + \Phi_o} \tag{A.6}$$

The Green's function $G(x, x')$ correlates the response Φ to the source $f(x)$.

[1] This step can be performed as $< \hat{D} >$ acts only on the x-dimension.

A.2 The Helmholtz Equation

Having some notion of the Green's function technique, we will now turn our attention to solving a differential form which may be used for electrodynamics. The Helmholtz equation is a differential equation for the function $\Psi(\vec{r})$ of the form

$$\left(\nabla^2 + k^2\right)\Psi(\vec{r}) = S(\vec{r}) \tag{A.7}$$

where $S(\vec{r})$ is some source function.

As an example of the powerful versatility of this equation, consider the well known Schrodinger's equation from quantum mechanics:

$$\left(\frac{-\hbar^2}{2m}\right)\nabla^2\Psi + V\Psi = E\Psi \tag{A.8}$$

where $\hbar$, m and E are all defined as per the convention of quantum mechanics, and V is a potential. May be given by the general Helmholtz form by making the substitution $k^2 = \frac{2mE}{\hbar^2}$,

$$\left(\nabla^2 + k^2\right)\Psi = \frac{2m}{\hbar^2}V\Psi = S(\vec{r}) \tag{A.9}$$

Following the outline dictated in the preceding subsection, in order to use the Green's function approach we must first find a solution to the equation

$$\left(\nabla^2 + k^2\right)g(\vec{r}, \vec{r'}) = \delta(\vec{r} - \vec{r'}) \tag{A.10}$$

Which, by taking $\vec{r'}$ to be at the origin, and performing a Fourier transform

$$g(r) = \iiint \frac{\mathrm{d}^3q}{(2\pi)^3}\tilde{g}(\vec{q})e^{i\vec{q}\cdot\vec{r}} \tag{A.11a}$$

$$\delta(\vec{r}) = \iiint \frac{\mathrm{d}^3q}{(2\pi)^3}e^{i\vec{q}\cdot\vec{r}} \tag{A.11b}$$

may be rearranged to produce

$$\iiint \frac{\mathrm{d}^3q}{(2\pi)^3}(-q^2 + k^2)\tilde{g}(\vec{q})e^{i\vec{q}\cdot\vec{r}} = \iiint \frac{\mathrm{d}^3}{(2\pi)^3}e^{i\vec{q}\cdot\vec{r}} \tag{A.12}$$

As this equation must hold for all k and q, we may equate the terms under the integral and solve for the fourier transform of the greens function, $\tilde{g}(\vec{q})$ as

$$\tilde{g}(q) = \frac{1}{k^2 - q^2} \tag{A.13}$$

and therefore, $g(r)$ can be expressed as

$$\iiint \frac{\mathrm{d}^3 q}{(2\pi)^3} \frac{1}{k^2 - q^2} e^{i\vec{q}\cdot\vec{r}} \tag{A.14}$$

By orienting $\vec{r}$ along the polar axis, switching to polar coordinates, and making use of the Cauchy integral formula [2], this result may be solved to yield the scalar green's function for the Helmholtz equation which can be used to solve any equation that may be placed in the Helmholtz form.

$$\boxed{g(r) = -\frac{e^{ikr}}{4\pi r}} \tag{A.15}$$

As an aside, by recalling the sample Schrodinger equation shown at the beginning of this section, and the formal way in which Green's functions solutions are used, we can easily recover a rather famous result. By simply plugging in our new solution and guessing an initial form for the particular solution $\Psi_o = e^{i\vec{k}\cdot\vec{r}}$ we recover the heralded Lippmann-Schwinger equation for a scattering potential:

$$\Psi = e^{i\vec{k}\cdot\vec{r}} + \int -\frac{e^{ik|r-r'|}}{4\pi\,|r-r'|} \frac{2m}{\hbar^2} V \Psi \mathrm{d}V' \tag{A.16}$$

A.2.1 Relating Maxwell's Equations to the Helmholtz Form

Recalling the standard differential forms of Maxwell's equation:

$$\vec{\nabla}\cdot\vec{D} = 4\pi\rho \tag{A.17}$$

$$\vec{\nabla}\cdot\vec{B} = 0 \tag{A.18}$$

$$\vec{\nabla}\times\vec{E} = -\frac{1}{c}\frac{\partial\vec{B}}{\partial t} \tag{A.19}$$

$$\vec{\nabla}\times\vec{H} = \frac{4\pi}{c}\vec{J} + \frac{1}{c}\frac{\partial\vec{D}}{\partial t} \tag{A.20}$$

and the potential definitions:

$$\vec{B} = \vec{\nabla}\times\vec{A} \tag{A.21}$$

$$\vec{E} = -\frac{1}{c}\frac{\partial\vec{A}}{\partial t} - \vec{\nabla}\phi \tag{A.22}$$

It is possible to cast Maxwell's equations into the familiar form of the Helmholtz equation. By taking the source free Maxwell's equation A.20 and subbing in the

[2] This step is done after having integrated both angular components and displacing the poles into the imaginary plane. ie.$(q - k - i\epsilon)(q + k + i\epsilon)$ The Cauchy integral formula may then be applied in the standard way.

appropriate potential formulations, described by equations A.21 and A.22, we get

$$\vec{\nabla} \times \left(\vec{\nabla} \times \vec{A} \right) = \frac{4\pi\mu}{c} \vec{J} + \frac{\epsilon\mu}{c^2} \frac{\partial}{\partial t} \left(-\frac{\partial \vec{A}}{\partial t} - \vec{\nabla}\phi c \right) \tag{A.23}$$

Which can then be manipulated by employing differential vector identities and making use of the Lorenz gauge[3] to return us to an equation of the Helmholtz form as follows.[4]

$$\nabla^2 \vec{A} - \frac{\epsilon\mu}{c^2} \frac{\partial^2 \vec{A}}{\partial t^2} = \frac{-4\pi\mu\vec{J}}{c} \tag{A.24}$$

$$\frac{\partial^2 \vec{A}}{\partial t^2} = -\omega^2 \vec{A} \tag{A.25}$$

$$\Rightarrow \boxed{\left(\nabla^2 \cdot + \epsilon\mu k_0^2 \right) \vec{A} = -\frac{4\pi\mu}{c} \vec{J}} \tag{A.26}$$

In turn, this result also allows us to solve for the electric field by noting the relation between the scalar and vector fields imposed by the Lorenz gauge and noting the potential relation A.22.

$$\vec{E} = -\frac{1}{c} \frac{\partial \vec{A}}{\partial t} \frac{1}{i\epsilon\mu k_0} \vec{\nabla} \left(\vec{\nabla} \cdot \vec{A} \right) \tag{A.27}$$

A.3 Green's Function for Electromagnetic Sources

As shown above, under the assumption of time harmonic fields, equation A.26 can be rewritten as:

$$(k_1^2 + \nabla^2 \cdot) \vec{A} = \frac{-4\pi\mu}{c} \vec{J} \tag{A.28}$$

Where $k_1^2 := \epsilon\mu k_0^2 = \frac{\epsilon\mu\omega^2}{c^2}$. This then leads to the formula for $\vec{E}$

$$\left(-k_1^2 + \vec{\nabla} \times \vec{\nabla} \times \right) \vec{E} = i \frac{4\pi\mu k_0}{c} \vec{J} \tag{A.29}$$

Therefore, by drawing from the arguments presented in the introduction we may now write

$$\left(-k_1^2 + \vec{\nabla} \times \vec{\nabla} \times \right) \bar{G}_x = i \frac{4\pi\mu k_0}{c} \vec{\delta_x} \tag{A.30}$$

By performing this computation in each direction (x, y, and z) we can determine the expression for the Dyadic Green's function for Electromagnetic sources and therefore

[3] The Lorenz gauge under time harmonic assumptions is $0 = \nabla \cdot \vec{A} - \epsilon\mu \frac{\partial \phi}{\partial t}$.

[4] We solve for $\vec{A}$ and not $\vec{E}$ as the vector identities required to reach a Helmholtz form for the electric field would severely limit the possible scope for which our formulation could be used.

arrive at a general result for computing electric fields due to a general source $\vec{J}$

$$\vec{E}(\vec{r}) = 0 + i\frac{4\pi\mu k_0}{c}\int \bar{G}\vec{J}\mathrm{d}V' \tag{A.31}$$

Recalling that an oscillating, and therefore radiating, point dipole positioned at $\vec{r'}$ and pointed in the direction $\vec{\mu}$ may be written as

$$\vec{\mu}(\vec{r},t) = \vec{\mu}\delta(\vec{r}-\vec{r'})e^{-i\omega t} \tag{A.32}$$

and that this approximately corresponds to a current of $\vec{J}(\vec{r},t) = \frac{\partial\vec{u}}{\partial t}$, by setting the phase of the dipole equal to unity we may conclude that[5]

$$\begin{aligned}\vec{E}(\vec{r}) &= i\frac{4\pi\mu\omega}{c^2}\int \bar{G}\left(\vec{r},\vec{r}\right)(-i\omega)\vec{\mu}\delta(\vec{r}-\vec{r}\,')\mathrm{d}V' \\ &= 4\pi\mu k_0^2\bar{G}\left(\vec{r},\vec{r}\right)\vec{\mu}\end{aligned} \tag{A.33}$$

As from the previous section we are aware that,

$$\vec{E} = ik_0\left[1+\frac{\vec{\nabla}\vec{\nabla}}{k_1^2}\right]\vec{A} \tag{A.34}$$

we may finally establish that a fixed form for our Dyadic Green's function is given by: [6]

$$\boxed{\bar{G} = \left[\bar{I}+\frac{\vec{\nabla}\vec{\nabla}}{k_1^2}\right]g(\vec{r})} \tag{A.35}$$

Where $g(\vec{r})$ is the Green's function of the Helmholtz equation. Which, following the derivation of the Weyl's identity, may be written as:

$$g(r) = -\frac{e^{ikr}}{4\pi r} = \frac{i}{8\pi^2}\iint_{-\infty}^{\infty}\mathrm{d}k_x\mathrm{d}k_y\frac{1}{k_z}e^{i(k_x x+k_y y+k_z|z|)} \tag{A.36}$$

We now have a useful form for finding extremely complicated electric fields due to general sources.

A.4 Simulating Point Sources and Numerical Methods

We have seen in the preceding sections that the electric field due to a radiating point dipole can be represented quite simply as $\vec{E} = \bar{G}\vec{\mu}$ where $\bar{G}$ is the dyadic green's function for Maxwell's equations, and $\vec{\mu}$ is the point dipole moment vector.

[5] μ denotes magnetic permeability, $\vec{\mu}$ the dipole moment.

[6] The $\vec{\nabla}$ operator acts to increase the dimension of the operand.

In addition, the dyadic green's function can be represented in operator form as

$$\bar{G} = \hat{O}\ \frac{e^{ikr}}{4\pi r} = \left(\bar{I} + \frac{\nabla\nabla}{k_1^2}\right)\frac{e^{ikr}}{4\pi r} \tag{A.37}$$

Written in exact component form, the operator $\hat{O}$ is

$$\hat{O} = \begin{pmatrix} 1+\frac{\partial_{xx}^2}{k_1^2} & \frac{\partial_{xy}^2}{k_1^2} & \frac{\partial_{xz}^2}{k_1^2} \\ \frac{\partial_{xy}^2}{k_1^2} & 1+\frac{\partial_{yy}^2}{k_1^2} & \frac{\partial_{yz}^2}{k_1^2} \\ \frac{\partial_{xz}^2}{k_1^2} & \frac{\partial_{yz}^2}{k_1^2} & 1+\frac{\partial_{zz}^2}{k_1^2} \end{pmatrix} \tag{A.38}$$

Our structures will have symmetry in the xy-plane and inhomogeneities in the z-direction. Therefore, if we chose our point dipole to be oriented along the z-direction, then all of the emitted radiation will be TM (p-pol) with respect to any plane oriented along the xy-direction. This corresponds to a dipole moment of

$$\vec{\mu} = \begin{pmatrix} 0 \\ 0 \\ 1 \end{pmatrix} \tag{A.39}$$

in this case, the radiated electric field is[7]

$$\vec{E} \sim \begin{pmatrix} \frac{\partial_{xz}^2}{k_1^2} \\ \frac{\partial_{yz}^2}{k_1^2} \\ 1+\frac{\partial_{zz}^2}{k_1^2} \end{pmatrix} \cdot \frac{e^{ikr}}{4\pi r} \tag{A.40}$$

To be able to model reflections and more complex structures, we will employ the Weyl identity to express $e^{ikr}/4\pi r$ as a sum of plane waves (equation A.36). However, when the vector operator (equation A.40) is applied to the Weyl Identity, there is no closed form for the integrals and, numerically, the integrals converge very slowly, making them very computationally inefficient.

In response, we will manipulate the Weyl identity to obtain a more numerically efficient form. The Weyl identity has a singularity when $k_x^2 + k_y^2 = k_1^2 \Rightarrow k_z = 0$. This is the point in the wave-vector spectrum at which the emitted waves from the point source switch from propagating waves to evanescent waves. We will therefore, decompose the Weyl indentity into two discrete components: the *homogenous* and *evanescent* parts. That is,

$$g(r) = g^H(r) + g^E(r) \tag{A.41a}$$

[7]The coefficient of $\frac{4\pi\mu\omega^2}{c^2}$ has been suppressed.

$$g^H(r) = \frac{i}{8\pi^2} \iint\limits_{k_x^2+k_y^2<k_1^2} \frac{1}{k_z} e^{i(k_x x + k_y y + k + z|z|)} \tag{A.41b}$$

$$g^E(r) = \frac{i}{8\pi^2} \iint\limits_{k_x^2+k_y^2>k_1^2} \frac{1}{k_z} e^{i(k_x x + k_y y + k + z|z|)} \tag{A.41c}$$

In the following two sections the algebraic manipulations of these two integral components will be outlined.

A.4.1 Homogeneous Component

We will start by making the substitution

$$k_\rho^2 := k_x^2 + k_y^2 \tag{A.42}$$

Then $k_x = k_\rho \cos(\theta)$ and $k_y = k_\rho \sin(\theta)$ for some θ. The integral representation of $g^H(r)$ then becomes

$$g^H(r) = \frac{i}{8\pi^2} \int_0^{k_1} \int_0^{2\pi} \mathrm{d}k_\rho \mathrm{d}\theta \frac{k_\rho}{\sqrt{k_1^2 - k_\rho^2}} e^{i\sqrt{k_1^2-k_\rho^2}|z|} e^{i(x k_\rho \cos\theta + y k_\rho \sin\theta)}$$

where θ runs from 0 to 2π and k_ρ runs from 0 to k_1.

Considering only the angular part of this integral, we have

$$I_\theta = \int_0^{2\pi} \mathrm{d}\theta e^{i(x k_\rho \cos\theta + y k_\rho \sin\theta)} \tag{A.43}$$

If we multiply the whole argument in the exponent by $\sqrt{x^2+y^2}/\sqrt{x^2+y^2}$ and employ a cosine double angle identity, we can reduce equation A.43 to the well known bessel form[8]

$$I_\theta = \int_0^{2\pi} \mathrm{d}\theta e^{i k_\rho \sqrt{x^2+y^2} \cos(\theta-\phi)} \tag{A.44}$$

$$= 2\pi J_0(k_\rho \sqrt{x^2+y^2}) \tag{A.45}$$

The total expression for $g^H(r)$ is now written as

$$g^H(r) = \frac{i}{4\pi} \int_0^{k_1} \mathrm{d}k_\rho \frac{k_\rho J_0(k_\rho \sqrt{x^2+y^2})}{\sqrt{k_1^2 - k_\rho^2}} e^{i\sqrt{k_1^2-k_\rho^2}|z|} \tag{A.46}$$

[8] $x/\sqrt{x^2+y^2} = \cos\phi$ and $y/\sqrt{x^2+y^2} = \sin\phi$

This is a single integrand expression for $g^H(r)$, however, it still has a singularity, namely as $k_\rho \to k_1$. We will effectively remove this singularity by changing the integral bounds from $(0, k_1)$ to $(0, 1)$. To do this we perform the change of variable

$$u := \sqrt{1 - k_\rho^2/k_1^2} \tag{A.47}$$

which yields the final form of the homogeneous part of the scalar Green's function

$$\boxed{g^H(r) = \frac{i}{4\pi k_1} \int_0^1 \mathrm{d}u \; J_0\left(k_1\sqrt{1-u^2}\sqrt{x^2+y^2}\right) e^{ik_1 u|z|}} \tag{A.48}$$

Note that the u is a unitless differential of integration.

A.4.2 Evanescent Component

For the evanescent part we have that $k_x^2 + k_y^2 > k_1^2$ so that the propagation wavevector k_z can be written as

$$k_z = i\sqrt{k_x^2 + k_y^2 - k_1^2} \tag{A.49}$$

Similar to the substitutions made in the *Homogeneous part* section, we let $k_\rho^2 := k_x^2 + k_y^2$ Then $g^E(r)$ is transformed from equation A.41c to

$$g^E(r) = \frac{1}{8\pi^2} \cdot \int_0^{k_1}\int_0^{2\pi} \mathrm{d}k_\rho \mathrm{d}\theta \frac{k_\rho}{\sqrt{k_\rho^2 - k_1^2}} e^{-\sqrt{k_\rho^2 - k_1^2}|z|} e^{i(xk_\rho\cos\theta + yk_\rho\sin\theta)} \tag{A.50}$$

By splitting the integrals into wavevector and angular parts, and making the exact same trigonometric substitution described in the preceding section, $g^E(r)$ can be rewritten as

$$g^E(r) = \frac{1}{4\pi}\int_{k_1}^{\infty} \mathrm{d}k_\rho \frac{k_\rho J_0\left(k_\rho\sqrt{x^2+y^2}\right)}{\sqrt{k_\rho^2 - k_1^2}} e^{-\sqrt{k_\rho^2 - k_1^2}|z|} \tag{A.51}$$

Again, this is a single integral, but it has a singularity as $k_\rho \to k_1$. We will effectively remove this singularity by performing the change of variable

$$v := \sqrt{k_\rho^2/k_1^2 - 1} \tag{A.52}$$

The final expression for $g^E(r)$ is then a unitless integrand with bounds $(0, \infty)$.

$$\boxed{g^E(r) = \frac{1}{4\pi k_1} \int_0^\infty \mathrm{d}v J_0 \left(k_1 \sqrt{v^2+1} \sqrt{x^2+y^2} \right) e^{-k_1 v |z|}} \tag{A.53}$$

Note: We will still have trouble near $z \approx 0$, as there will be very little "damping", as $e^{-k_1 v|z|} \approx 1$, and the integral will converge very slowly (numerically).

A.4.3 The Fields of a Radiating Point Dipole Oriented Along the z-axis

We can now apply the operator shown in equation A.40. The exact algebra will not be shown here, but rather, the results will be stated. The x, y, and z components all have homogeneous and evanescent parts. The following are the integral representation for the time harmonic electric fields due to a radiating point dipole. The integrals are no longer summations of a spectrum of plane waves, but rather a summation of a spectrum of cylindrical waves. On a historical note, these are referred to as Sommerfeld integrals due to his work on a similar problem, radio frequency antennas and surface waves.

$$E_x^H \sim \mp \frac{1}{4\pi k_1} \frac{x}{\sqrt{x^2+y^2}} \int_0^1 u\sqrt{1-u^2} J_0' \left(k_1 \sqrt{1-u^2} \sqrt{x^2+y^2} \right) e^{ik_1 u|z|} \mathrm{d}u \tag{A.54}$$

$$E_x^E \sim \mp \frac{1}{4\pi k_1} \frac{x}{\sqrt{x^2+y^2}} \int_0^\infty v\sqrt{1+v^2} J_0' \left(k_1 \sqrt{1+v^2} \sqrt{x^2+y^2} \right) e^{-k_1 v|z|} \mathrm{d}v \tag{A.55}$$

$$E_y^H \sim \mp \frac{1}{4\pi k_1} \frac{x}{\sqrt{x^2+y^2}} \int_0^1 u\sqrt{1-u^2} J_0' \left(k_1 \sqrt{1-u^2} \sqrt{x^2+y^2} \right) e^{ik_1 u|z|} \mathrm{d}u \tag{A.56}$$

$$E_y^E \sim \mp \frac{1}{4\pi k_1} \frac{x}{\sqrt{x^2+y^2}} \int_0^\infty v\sqrt{1+v^2} J_0' \left(k_1 \sqrt{1+v^2} \sqrt{x^2+y^2} \right) e^{-k_1 v|z|} \mathrm{d}v \tag{A.57}$$

$$E_z^H \sim \frac{i}{4\pi k_1} \int_0^1 \left(1-u^2\right) J_0 \left(k_1 \sqrt{1-u^2} \sqrt{x^2+y^2} \right) e^{ik_1 u|z|} \mathrm{d}u \tag{A.58}$$

$$E_z^E \sim \frac{1}{4\pi k_1} \int_0^\infty (1+v^2) J_0 \left(k_1 \sqrt{1+v^2} \sqrt{x^2+y^2} \right) e^{-k_1 v|z|} \mathrm{d}v \tag{A.59}$$

Note: The x and y integrals are functions of the derivative of the bessel function J_0', where as in the z case it is not.

A.5 Radiated Fields Near A Planar Interface

Let us now consider the geometry with a point dipole above a planar uniaxial medium. Let the dipole be oriented along at z-axis and be a distance d above the surface of the planar interface. If the dipole is closer than about $\sim \lambda$ to the interface, evanescent fields from the dipole will interact with the second structure and thereby excite other modes of radiation.

If we interpret the Green's function approach outlined earlier as a summation of plane waves, then we can treat this problem quite well using Fresnel reflection and transmission. Since a point dipole oriented normal to the surface will emit only TM polarized waves, then we need only consider the TM or p-polarized reflection and transmission coefficients, $r_e(k_x, k_y)$ and $t_e(k_x, k_y)$.[9] Noting that the fresnel reflection and transmission coefficients do not depend on the spatial coordinates (x, y, z) on which the operator $\hat{O}$ acts on in equation A.37, we can then use r_e and t_e under the integrals shown in equations A.70 through A.81, to obtain the incident and reflected fields, provided we make the same change of variables etc, as used in the derivations above.

Since the dipole is now located at $z = d$ and not the origin, we must displace the original incident electric field equations by $-d$ in the z-direction.

$$z \to z - d \tag{A.60}$$

The form of the incident electric fields are then the exact same as those shown in equations A.70 through A.81 with this change of variable in the z variable. The incident fields are defined for $z > 0$.

Recall that we made the change of variable $k_\rho^2 = k_x^2 + k_y^2$ in the electric field derivations and then further converted k_ρ to an expression for u and v for the homogeneous and evanescent cases respectively. In the homogeneous case this corresponds to

$$k_\rho^2 = k_1^2 \left(1 - u^2\right) \tag{A.61}$$

and in the evanescent case this corresponds to

$$k_\rho^2 = k_1^2 \left(1 + v^2\right) \tag{A.62}$$

In the equations for r_e and t_e, we can change then alter the expressions for $k_{z,i}$ and

[9] I use the subscript e here because TM polarized waves correspond to extraordinary waves inside the uniaxial medium; this is just convention.

$k_{z,t}$ to conform to our new expressions for k_ρ^2. The incident k_Z becomes

$$k_{z,i}(u) = k_1 u;\ \textit{homogeneous case} \tag{A.63}$$

$$k_{z,i}(v) = ik_1 v;\ \textit{evanescent case} \tag{A.64}$$

and the transmitted k_z becomes

$$k_{z,t}(u) = k_0\sqrt{\epsilon_{||}\left(1-\frac{\epsilon_1}{\epsilon_\perp}(1-u^2)\right)};\ \textit{homogeneous case} \tag{A.65}$$

$$k_{z,t}(v) = k_0\sqrt{\epsilon_{||}\left(1-\frac{\epsilon_1}{\epsilon_\perp}(1+v^2)\right)};\ \textit{evanescent case} \tag{A.66}$$

$$\tag{A.67}$$

and we still have

$$r_e(u \text{ or } v) = \frac{\epsilon_{||}k_{z,i}-\epsilon_1 k_{z,t}}{\epsilon_{||}k_{z,i}+\epsilon_1 k_{z,t}} \tag{A.68}$$

$$t_e(u \text{ or } v) = \frac{2\epsilon_{||}k_{z,i}}{\epsilon_{||}k_{z,i}+\epsilon_1 k_{z,t}}\sqrt{\frac{\epsilon_1}{\epsilon_{||}}} \tag{A.69}$$

The reflected fields will then have the form (for $z>0$)

$$E^H_{x,ref} \sim -\frac{1}{4\pi k_1}\frac{x}{\sqrt{x^2+y^2}}\int_0^1 r_e(u)u\sqrt{1-u^2}J_0'\left(k_1\sqrt{1-u^2}\sqrt{x^2+y^2}\right)e^{ik_1u(z+d)}\mathrm{d}u \tag{A.70}$$

$$E^E_{x,ref} \sim -\frac{1}{4\pi k_1}\frac{x}{\sqrt{x^2+y^2}}\int_0^\infty r_e(v)v\sqrt{1+v^2}J_0'\left(k_1\sqrt{1+v^2}\sqrt{x^2+y^2}\right)e^{-k_1v(z+d)}\mathrm{d}v \tag{A.71}$$

$$E^H_{y,ref} \sim -\frac{1}{4\pi k_1}\frac{y}{\sqrt{x^2+y^2}}\int_0^1 r_e(u)u\sqrt{1-u^2}J_0'\left(k_1\sqrt{1-u^2}\sqrt{x^2+y^2}\right)e^{ik_1u(z+d)}\mathrm{d}u \tag{A.72}$$

$$E^E_{y,ref} \sim -\frac{1}{4\pi k_1}\frac{y}{\sqrt{x^2+y^2}}\int_0^\infty r_e(u)r_e(v)v\sqrt{1+v^2}J_0'\left(k_1\sqrt{1+v^2}\sqrt{x^2+y^2}\right)e^{-k_1v(z+d)}\mathrm{d}v \tag{A.73}$$

$$E^H_{z,ref} \sim \frac{i}{4\pi k_1}\int_0^1 r_e(u)\left(1-u^2\right)J_0\left(k_1\sqrt{1-u^2}\sqrt{x^2+y^2}\right)e^{ik_1u(z+d)}\mathrm{d}u \tag{A.74}$$

$$E^E_{z,ref} \sim \frac{1}{4\pi k_1}\int_0^\infty r_e(v)(1+v^2)J_0\left(k_1\sqrt{1+v^2}\sqrt{x^2+y^2}\right)e^{-k_1v(z+d)}\mathrm{d}v \tag{A.75}$$

Similarly, the transmitted fields will have the form (for $z < 0$)

$$E^H_{x,trans} \sim +\frac{1}{4\pi k_1}\frac{x}{\sqrt{x^2+y^2}}\int_0^1 t_e(u)u\sqrt{1-u^2}J_0'\left(k_1\sqrt{1-u^2}\sqrt{x^2+y^2}\right)e^{ik_1ud}e^{-ik_{z,t}(u)z}\mathrm{d}u \tag{A.76}$$

$$E^E_{x,trans} \sim +\frac{1}{4\pi k_1}\frac{x}{\sqrt{x^2+y^2}}\int_0^\infty t_e(v)v\sqrt{1+v^2}J_0'\left(k_1\sqrt{1+v^2}\sqrt{x^2+y^2}\right)e^{-k_1vd}e^{-ik_{z,t}(v)z}\mathrm{d}v \tag{A.77}$$

$$E^H_{y,trans} \sim +\frac{1}{4\pi k_1}\frac{y}{\sqrt{x^2+y^2}}\int_0^1 t_e(u)u\sqrt{1-u^2}J_0'\left(k_1\sqrt{1-u^2}\sqrt{x^2+y^2}\right)e^{ik_1ud}e^{-ik_{z,t}(u)z}\mathrm{d}u \tag{A.78}$$

$$E^E_{y,trans} \sim +\frac{1}{4\pi k_1}\frac{y}{\sqrt{x^2+y^2}}\int_0^\infty t_e(v)v\sqrt{1+v^2}J_0'\left(k_1\sqrt{1+v^2}\sqrt{x^2+y^2}\right)e^{-k_1vd}e^{-ik_{z,t}(v)z}\mathrm{d}v \tag{A.79}$$

$$E^H_{z,trans} \sim \frac{i}{4\pi k_1}\int_0^1 t_e(u)\left(1-u^2\right)J_0\left(k_1\sqrt{1-u^2}\sqrt{x^2+y^2}\right)e^{ik_1ud}e^{-ik_{z,t}(u)z}\mathrm{d}u \tag{A.80}$$

$$E^E_{z,trans} \sim \frac{1}{4\pi k_1}\int_0^\infty t_e(v)(1+v^2)J_0\left(k_1\sqrt{1+v^2}\sqrt{x^2+y^2}\right)^{-k_1vd}e^{-ik_{z,t}(v)z}\mathrm{d}v \tag{A.81}$$

A.6 Semi Classical Theory of Spontaneous Emission

A.6.1 Introduction

Building off the results of the previous section we are now in a position to use the Green's function formalism to determine the lifetime of a spontaneous emitter, such as a simple system with two quantized energy levels.

Recalling Fermi's Golden rule:

$$\Gamma_s = \frac{2\pi}{\hbar}\left|\langle\Psi_f\left|H_{int}\right|\Psi_i\rangle\right|^2 n(\epsilon_f) \tag{A.82}$$

(Where Ψ is used to represent quantum states, $n(\epsilon_f)$ the final density of states, H the Hamiltonian of the system and Γ the rate of decay of the system.)

It quickly becomes clear that the lifetime of an excited state relies heavily on the density of final available states to the excitation; or, from an anthropomorphic perspective, the likelihood of a transition to another state depends on how much space the excitation knows is available at that particular energy. If we now make use of semi-classical techniques, we can deduce from arguments about the proportionality

of the density of states that

$$\Gamma = \frac{P}{\hbar\omega} \tag{A.83}$$

(where P is the average power emitted from the system).

A.6.2 Lifetime of a Spontaneous Emitter Dipole

Using the Green's function result from equation A.33 along with knowledge from classical electrodynamics that

$$\langle P \rangle = \int \frac{1}{2}\mathrm{Re}\left(\vec{J}^* \cdot \vec{E}\right) \mathrm{d}V' \tag{A.84}$$

we can now determine the average power emitted by a dipole. Using a time harmonic approach, identical to the one used in the preceding section, we will assume that the dipole produces a current of

$$\vec{J} = -i\omega\vec{\mu}e^{-i\omega t}\delta(\vec{r} - \hat{z}d) \tag{A.85}$$

Which then leads to the result:

$$\langle P \rangle = \int \frac{1}{2}\mathrm{Re}\left[i\omega\vec{\mu}^* \left(\frac{\omega}{c}\right)^2 \delta(\vec{r} - \vec{r_o})4\pi\mu G(\vec{r}, \vec{r_o})\vec{\mu}\right] \mathrm{d}V' \tag{A.86}$$

$$\langle P \rangle = \frac{2\pi\mu\omega^3}{c^2}\mathrm{Im}\left[\vec{\mu}^* \cdot \bar{G}(\vec{r_o}, \vec{r_o}) \cdot \vec{\mu}\right] \tag{A.87}$$

with $\bar{G}$ given by

$$\bar{G} = \left[\bar{I} + \frac{\vec{\nabla}\vec{\nabla}}{k_1^2}\right]\left(\frac{i}{8\pi^2}\iint_{-\infty}^{\infty} \mathrm{d}k_x \mathrm{d}k_y \frac{1}{k_z} e^{i(k_x x + k_y y + k_z|z|)}\right) \tag{A.88}$$

If we orient our space such that the dipole is oriented along a single direction, say the $\hat{z}$ direction, and is positioned at the origin,A.88 may be solved by the aid of trigonometric substitutions to yield:

$$\boxed{\langle P \rangle = \frac{n\mu\omega^4}{3c^3}\left|\vec{\mu}\right|^2} \tag{A.89}$$

where n is the index of refraction, and $|\vec{\mu}|$ is the magnitude of the dipole vector. All other symbols follow the standard convention. *Note* that this is the famous Larmor formula but with an added corrective factor of μ. This correction is very important for negative index materials.

A.6.3 Lifetime of a Spontaneous Emitter in the Presence of a Planar Material

Given the manner and formalism of the previous subsection, calculating the lifetime of a spontaneous emitter in the presence of material is actually much simpler than one might initially think. As we must only consider the Green's function at the location of the current, in this case the dipole, in order to calculate the emitted power, and associated decay rate, our tasked is simplified to determining the electric field at the position of the dipole. Thus, the only change that must be made to the conclusions of the previous subsection is to replace free emission electric field by:

$$\vec{E} = 4\pi \left(\frac{\omega}{c}\right)^2 (\bar{G}_{free} + \bar{G}_{ref}) \cdot \vec{\mu} \tag{A.90}$$

Where $\bar{G}_{free}$ is identical to the Green's function presented in the previous subsection, and $\bar{G}_{ref}$ is defined using the p-polarization (TM) reflection coefficient r_p as $\bar{G}_{ref} = r_p \bar{G}_{inc}$.[10]

Drawing from the previous subsection, and normalizing the power with result from equation A.89, leads us to the conclusion that the normalized decay rate of a spontaneous emitter a distance d from a planar interface is found to be:

$$\boxed{\frac{\Gamma}{\Gamma_o} \propto \frac{P}{P_o} = 1 + \frac{3}{2}\mathrm{Re}\left[\int_0^\infty r_p(s)\frac{s^3}{s_z}e^{i2s_z k_0 d}\mathrm{d}s\right]} \tag{A.91}$$

Where d is the distance of the dipole, $r_p(s)$ the P reflection coefficient as a function of s, and the various s as well as wave vectors (k's) by the equation:

$$s^2 = \frac{k_x^2 + k_y^2}{k_0^2} \tag{A.92a}$$

$$s_z^2 = \frac{k_z^2}{k_0^2} \tag{A.92b}$$

A.6.4 Numerical Techniques for Calculating the Lifetime of a Spontaneous Emitter Near a Planar Material

Numerical study of the result of the previous subsection A.91 is much simpler than the general field techniques presented in section A.4. After separating the integral into propagating and evanescent components as detailed in the earlier numerical subsection, our only major concern is setting an upper limit on the evanescent waves to consider. This is perhaps done most simply by considering the decay constant of

[10] As described earlier, a dipole oriented perpendicular to an interface will emit only p-polarized light (TM) with respect to that interface.

the evanescent integral given by

$$e^{-2k_0 s_z d} \tag{A.93}$$

Once the exponent of this quantity reaches a large negative number, say -30 for example, it becomes very unlikely that the reflection coefficient will be large enough to make a meaningful contribution to the integral. Thus, recalling the earlier definition of s (A.92a), we can quickly determine a reasonable upper cut off for the integral in the evanescent case as

$$\left(k_x^2 - k_0^2\right)^{1/2} = \frac{15}{d} \tag{A.94}$$

$$\Rightarrow \left(\frac{k_x}{k_0}\right)_{\text{cutoff}} = \left[\left(\frac{15}{k_0 d}\right)^2 + 1\right]^{1/2} \tag{A.95}$$

Appendix B

The Transfer Matrix Method

B.1 Introduction

We begin by motivating that a simple way to produce a hyperbolic metamaterial involves creating a multilayer stack of alternating metal and dielectric layers. Zeroth order *Maxwell-Garnett* effective medium theory accurately predicts that if the layer thickness is sub-wavelength then the bulk response of the multilayer system may exhibit extreme anisotropy (i.e. metallic in one direction and dielectric in another direction) corresponding to a hyperbolic isofrequency curve. Furthermore, alternating layers of high-index / low-index dielectrics with layer thicknesses $\approx \lambda/4n$ can give rise to a one-dimensional photonic bandgap. Here n = refractive index of each layer.

In order to test this prediction, we can extend the ideas found from the Fresnel coefficients at a single interface to that of a multilayer system. Unfortunately, the conventional method for solving even simple case of a single layer requires the summation of an infinite amount reflections inside of the slab itself. This method is called Airy Summation. Therefore, one can imagine that extending this concept to a multilayer system would result in quite an arduous and cumbersome process that would be nearly impossible to solve using the Airy summation technique. Instead, we exploit the simple electromagnetic boundary conditions at each interface of the multilayer. Here we show that by exploiting the fact that the tangential components of the magnetic and electric field must be continuous across any planar boundary, we can relate the fields at any interface to any other interface contained in the multilayer. The operation is performed through a *transfer matrix* technique and it can be used to calculate the reflection and transmission of an arbitrarily complex multilayer system. The technique shown here is general enough to handle so called high-k evanescent waves so that this method can predict the location of dielectric waveguide modes and metallic plasmonic modes.

B.2 Transfer Matrix Formulation

From Figure 1, we may visualize the general multilayer system consisting of layers with dielectric constant ϵ_i and thickness d_i. It is assumed that the films have infinite extent in both the x- and y-directions.

The goal of the Transfer Matrix Method is to relate the the incident and reflected fields to the transmitted fields using a single *Transfer Matrix*. This Transfer Matrix will contain all the information contained within the constituent layers.

We will develop the formulation for p-polarized light, however, the result can be easily translated to the s-polarized case as well, which we will explicitly give at the end.

Due to the cylindrical symmetry, without a loss of generality we assume the wave has no transverse momentum in the y-direction. That is the propagation wavevector is $\boldsymbol{k} = k_x\hat{x} + k_z\hat{z}$ where k_x^i and k_z^i are the projections of the propagation wavevector along the x- and z-directions respectively. They are related using the iso-frequency relation

$$k_x^2 + k_z^2 = \epsilon(\omega/c)^2. \tag{B.1}$$

If $k_x^2 > \epsilon(\omega/c)^2$, we must ensure that the imaginary part of k_z is positive: $\mathrm{Im}[k_z] > 0$ so that amplitudes of the electric and magnetic fields decay as they propagate.

P-polarized light only has a magnetic field in the y-direction such that in the ith layer the magnetic field can be written as $\boldsymbol{H^i} = H_y^i\hat{y}$ with

$$H_y^i = a_+^i \mathrm{e}^{j(k_x^i x + k_z^i z)} + a_-^i \mathrm{e}^{j(k_x^i x - k_z^i z)}. \tag{B.2}$$

That is, the ith layer supports both a forward and backward propagating wave. $a_\pm^i$ are the amplitudes of the forward and reverse propagating waves; note that these amplitudes are complex quantities.

Using Maxwell's equations we can relate the x-component of the electric field to the magnetic field as

$$E_x^i = \frac{k_z^i}{\epsilon_i k_o} a_+^i \mathrm{e}^{j(k_x^i x + k_z^i z)} + \frac{-k_z^i}{\epsilon_i k_o} a_-^i \mathrm{e}^{j(k_x^i x - k_z^i z)}, \tag{B.3}$$

where $k_o = \omega/c = 2\pi/\lambda$.

The electromagnetic boundary conditions at an interface require the components of the magnetic and electric field parallel to the interface, $\boldsymbol{H}_\parallel$ and $\boldsymbol{E}_\parallel$, be continuous across the boundary. For these conditions to be satisfied for all x, y we require that $k_x = k_x^i \ \forall i$. That is the transverse wavevector k_x is conserved for the whole system.

Therefore, for the ith interface $z = z_i$ and the boundary conditions require

$$E_x^i \big|_{z=z_i} = E_x^{i+1} \big|_{z=z_i} \tag{B.4}$$
$$H_y^i \big|_{z=z_i} = H_y^{i+1} \big|_{z=z_i}. \tag{B.5}$$

Cancelling out the common terms, the boundary conditions for the ith interface can be simplified to:

$$a_+^i e^{jk_z^i z_i} + a_-^i e^{-jk_z^i z_i} = a_+^{i+1} e^{jk_z^{i+1} z_i} + a_-^{i+1} e^{-jk_z^{i+1} z_i} \tag{B.6}$$
$$\frac{k_z^i}{\epsilon_i} a_+^i e^{jk_z^i z_i} - \frac{k_z^i}{\epsilon_i} a_-^i e^{-jk_z^i z_i} = \frac{k_z^{i+1}}{\epsilon_{i+1}} a_+^{i+1} e^{jk_z^{i+1} z_i} - \frac{k_z^{i+1}}{\epsilon_{i+1}} a_-^{i+1} e^{-jk_z^{i+1} z_i}. \tag{B.7}$$

It is convenient to rewrite this result above in simple matrix form.

$$\begin{pmatrix} 1 & 1 \\ \frac{k_z^i}{\epsilon_i} & -\frac{k_z^i}{\epsilon_i} \end{pmatrix} \begin{pmatrix} e^{jk_z^i z_i} & 0 \\ 0 & e^{-jk_z^i z_i} \end{pmatrix} \begin{pmatrix} a_+^i \\ a_-^i \end{pmatrix} = \begin{pmatrix} 1 & 1 \\ \frac{k_z^{i+1}}{\epsilon_{i+1}} & -\frac{k_z^{i+1}}{\epsilon_{i+1}} \end{pmatrix} \begin{pmatrix} e^{jk_z^{i+1} z_i} & 0 \\ 0 & e^{-jk_z^{i+1} z_i} \end{pmatrix} \begin{pmatrix} a_+^{i+1} \\ a_-^{i+1} \end{pmatrix} \tag{B.8}$$

Eqn. (3) can be rewritten in a more compact notation as

$$D_i p_i \begin{pmatrix} a_+^i \\ a_-^i \end{pmatrix} = D_{i+1} p_{i+1} \begin{pmatrix} a_+^{i+1} \\ a_-^{i+1} \end{pmatrix} \tag{B.9}$$

Additionally, this formulation can be extended to the $z = z_{i+1}$ interface such that

$$D_{i+1} p_{i+1} \begin{pmatrix} a_+^{i+1} \\ a_-^{i+1} \end{pmatrix} = D_{i+2} p_{i+2} \begin{pmatrix} a_+^{i+2} \\ a_-^{i+2} \end{pmatrix}. \tag{B.10}$$

Using the previous two equations we can relate the complex amplitudes of the ith layer to those of the $i+2$th layer.

$$\begin{aligned} \begin{pmatrix} a_+^i \\ a_-^i \end{pmatrix} = & \begin{pmatrix} e^{jk_z^i z_i} & 0 \\ 0 & e^{-jk_z^i z_i} \end{pmatrix}^{-1} \begin{pmatrix} 1 & 1 \\ \frac{k_z^i}{\epsilon_i} & -\frac{k_z^i}{\epsilon_i} \end{pmatrix}^{-1} \begin{pmatrix} 1 & 1 \\ \frac{k_z^{i+1}}{\epsilon_{i+1}} & -\frac{k_z^{i+1}}{\epsilon_{i+1}} \end{pmatrix} \begin{pmatrix} e^{jk_z^{i+1} z_i} & 0 \\ 0 & e^{-jk_z^{i+1} z_i} \end{pmatrix} \\ & \begin{pmatrix} e^{jk_z^{i+1} z_{i+1}} & 0 \\ 0 & e^{-jk_z^{i+1} z_{i+1}} \end{pmatrix}^{-1} \begin{pmatrix} 1 & 1 \\ \frac{k_z^{i+1}}{\epsilon_{i+1}} & -\frac{k_z^{i+1}}{\epsilon_{i+1}} \end{pmatrix}^{-1} \begin{pmatrix} 1 & 1 \\ \frac{k_z^{i+2}}{\epsilon_{i+2}} & -\frac{k_z^{i+2}}{\epsilon_{i+2}} \end{pmatrix} \begin{pmatrix} a_+^{i+2} \\ a_-^{i+2} \end{pmatrix} \end{aligned}$$

or equivalently,

$$\begin{pmatrix} a_+^i \\ a_-^i \end{pmatrix} = p_i^{-1} D_i^{-1} D_{i+1} P_{i+1} D_{i+1}^{-1} D_{i+2} p_{i+2} \begin{pmatrix} a_+^{i+2} \\ a_-^{i+2} \end{pmatrix} \tag{B.11}$$

Here, P_{i+1} is the combination of the fourth and fifth matrices on the right hand side of the equation – it will be written explicitly at the end of this section. Now, we

may continue the same procedure as above by extending the formulation from the $i = 0$ layer all the way to the $i = N$ layer as in Figure 1. In this way we **transfer** the boundary conditions from the $i = 0$ to the $i = N$ interface.[1]

$$\begin{pmatrix} a_+^0 \\ a_-^0 \end{pmatrix} = p_0^{-1} D_0^{-1} \left(\prod_{i=1}^{N} D_i P_i D_i^{-1} \right) D_{N+1} p_{N+1} \begin{pmatrix} a_+^{N+1} \\ a_-^{N+1} \end{pmatrix} \tag{B.12}$$

Finally, if we define the first interface as the origin ($z_0 = 0$) and use the physical fields for the outer regions (incident and reflected wave for incident medium, and only a transmitted outgoing wave in the final medium) then the general result for p-polarized (and s-polarized) light is given by[2]

$$\boxed{\begin{pmatrix} 1 \\ r^{s,p} \end{pmatrix} = (D_0^{s,p})^{-1} T^{s,p} D_{N+1}^{s,p} \begin{pmatrix} t^{s,p} \\ 0 \end{pmatrix}} \tag{B.13}$$

where

$$T^{s,p} = \left(\prod_{i=1}^{N} D_i^{s,p} P_i (D_i^{s,p})^{-1} \right) \tag{B.14}$$

and

$$D_i^p = \begin{pmatrix} 1 & 1 \\ \frac{k_z^i}{\epsilon_i} & -\frac{k_z^i}{\epsilon_i} \end{pmatrix}, D_i^s = \begin{pmatrix} 1 & 1 \\ k_z^i & -k_z^i \end{pmatrix}, P_i = \begin{pmatrix} e^{-jk_z^i d_i} & 0 \\ 0 & e^{jk_z^i d_i} \end{pmatrix}. \tag{B.15}$$

The reflection and transmission coefficients are given by the following simple result:

$$r^{s,p} = \frac{M_{21}^{s,p}}{M_{11}^{s,p}} \tag{B.16}$$

$$t^{s,p} = \frac{1}{M_{11}^{s,p}} \tag{B.17}$$

where M is total transfer matrix equal to $(D_0^{s,p})^{-1} T^{s,p} D_{N+1}^{s,p}$.

[1] One may simply perform the substitutions $i \to 0, i+1 \to i$, $i+2 \to N+1$ to obtain the result in Eqn. (8) as a shortcut.

[2] Eqn. (9) lacks the p_{N+1} term because it has been multiplied into the definition of $t^{s,p}$ as a simplification step.